Rapid Sea Level Rise in the Southern Hemisphere Subtropical Oceans

JING DUAN,[a,b] YUANLONG LI,[a,b] FAN WANG,[a,b] AIXUE HU,[c] WEIQING HAN,[d] LEI ZHANG,[d] PENGFEI LIN,[e] NAN ROSENBLOOM,[c] AND GERALD A. MEEHL[c]

[a] *CAS Key Laboratory of Ocean Circulation and Waves, Institute of Oceanology and Center for Ocean Mega-Science, Chinese Academy of Sciences, Qingdao, China*
[b] *Function Laboratory for Ocean Dynamics and Climate, Qingdao National Laboratory for Marine Science and Technology, Qingdao, China*
[c] *Climate and Global Dynamics Laboratory, National Center for Atmospheric Research, Boulder, Colorado*
[d] *Department of Atmospheric and Oceanic Sciences, University of Colorado, Boulder, Colorado*
[e] *LASG, Institute of Atmospheric Physics, Chinese Academy of Sciences, Beijing, China*

(Manuscript received 30 March 2021, in final form 15 July 2021)

ABSTRACT: The subtropical oceans between 35° and 20°S in the Southern Hemisphere (SH) have exhibited prevailingly rapid sea level rise (SLR) rates since the mid-twentieth century, amplifying damages of coastal hazards and exerting increasing threats to South America, Africa, and Australia. Yet, mechanisms of the observed SLR have not been firmly established, and its representation in climate models has not been examined. By analyzing observational sea level estimates, ocean reanalysis products, and ocean model hindcasts, we show that the steric SLR of the SH subtropical oceans between 35° and 20°S is faster than the global mean rate by 18.2% ± 9.9% during 1958–2014. However, present climate models—the fundamental bases for future climate projections—generally fail to reproduce this feature. Further analysis suggests that the rapid SLR in the SH subtropical oceans is primarily attributable to the persistent upward trend of the southern annular mode (SAM). Physically, this trend in SAM leads to the strengthening of the SH subtropical highs, with the strongest signatures observed in the southern Indian Ocean. These changes in atmospheric circulation promote regional SLR in the SH subtropics by driving upper-ocean convergence. Climate models show systematic biases in the simulated structure and trend magnitude of SAM and significantly underestimate the enhancement of subtropical highs. These biases lead to the inability of models to correctly simulate the observed subtropical SLR. This work highlights the paramount necessity of reducing model biases to provide reliable regional sea level projections.

KEYWORDS: Ocean; Indian Ocean; Dynamics; Sea level

1. Introduction

Estimates from tide gauge records and sea level reconstructions suggest that the global mean sea level has risen at an average rate of ~1.5 mm yr^{-1} since the early twentieth century, owing to ocean thermal expansion and land ice mass loss associated with anthropogenic greenhouse gas warming (e.g., Oppenheimer et al. 2019; Hay et al. 2015; Dangendorf et al. 2019; Frederikse et al. 2020), and is projected to rise further into the future (e.g., Jevrejeva et al. 2014; Slangen et al. 2017; Oppenheimer et al. 2019). The rate of sea level rise (SLR) is geographically heterogeneous as a result of regional processes such as alterations in atmospheric and oceanic circulations (e.g., Han et al. 2010, 2014; Stammer and Hüttemann 2008; Milne et al. 2009; Qiu and Chen 2012; Merrifield 2011; Thompson and Merrifield 2014). An enhanced regional SLR severely worsens the damages of coastal hazards, increasing the risks of permanent and irreversible inundation, land erosion, soil and groundwater salinization, property and infrastructure destruction, and storm surge inland penetration in low-lying coastal zones (e.g., Oppenheimer et al. 2019; Hauer et al. 2020). Therefore, scientific attribution of the observed regional SLR is pivotal to better support prediction and adaptation efforts.

Several recent studies have reported the prevailingly large SLR rates in the Southern Hemisphere (SH) subtropical oceans between 35° and 20°S during the past two to three decades (e.g., Jyoti et al. 2019; Qu et al. 2019; Qiu and Chen 2006; Roemmich et al. 2016). Longer records from tide gauge and sea level reconstructions also suggest an overall rapid subtropical SLR between 35° and 20°S since the mid-twentieth century (Han et al. 2010; Meyssignac et al. 2012; Kumar et al. 2020; Frederikse et al. 2020). In combination with extreme weather hazards, the enhanced regional SLR in the SH has entailed striking life and economic losses along the coasts of South America, Africa, and Australia (e.g., Oppenheimer et al. 2019; Duvat 2019). The 35°–20°S band is also where the subtropical circulation gyres are located, and the regional SLRs have implications for changes of these circulation gyres. However, in comparison with other regions such as the tropics, the northern Pacific and Atlantic Oceans, and the Southern Ocean south of 35°S, this latitude range has received relatively less attention from the sea level research community, and as a result the mechanisms have not been firmly established.

Existing studies have suggested strong modulation effects by tropical climate variability modes such as El Niño–Southern Oscillation (ENSO) on the subtropical oceans of the SH (e.g., Alexander et al. 2002; Lee and McPhaden 2008), and recent studies have underpinned an important role played by interbasin climate interactions through both atmospheric and oceanic teleconnections (e.g., Cai et al. 2019; Wang 2019).

Corresponding author: Yuanlong Li, liyuanlong@qdio.ac.cn

DOI: 10.1175/JCLI-D-21-0248.1

Particularly, low-frequency variability of the Indonesian Throughflow (ITF), as dictated by ENSO and its decadal modulation, can induce prominent sea level changes in the subtropical southern Indian Ocean (SIO) (e.g., Feng 2004; Schwarzkopf and Böning 2011; Trenary and Han 2013; Zhuang et al. 2013; Li et al. 2017; Jyoti et al. 2019; Volkov et al. 2020; Zhang et al. 2018; Lee et al. 2015; Nagura and McPhaden 2021). Recent studies have also revealed a notable forcing effect by the Southern Ocean climate, with the southern annular mode (SAM) as the leading variability mode (Trenberth 1979), on multidecadal changes of subtropical ocean circulation and sea level (e.g., Qu et al. 2019; Roemmich et al. 2016; Yang et al. 2020). There are also model-based results showing that stochastic processes, such as atmospheric weather perturbations and oceanic internal instabilities, may also leave considerable rectification effects on sea level variations on decadal and longer time scales in the subtropics, particularly in eddy-rich frontal zones under high storm-track activities (e.g., Qiu et al. 2015; Li and Han 2015; Sérazin et al. 2016). Under the above-mentioned candidate influences, causes for the regional SLR in the SH subtropics are difficult to fathom. Compared with the SLR of the southern Pacific and Atlantic Oceans reported by a number of recent studies (e.g., Vianna and Menezes 2013; Roemmich et al. 2015, 2016; Llovel and Terray 2016; Volkov et al. 2017; Frederikse et al. 2021), the SLR of the SIO is more complex in dynamics owing to the modulation effect from the Pacific via the ITF (e.g., Jyoti et al. 2019; Sprintall et al. 2014; Schwarzkopf and Böning 2011) and requires in-depth investigation.

The representation of long-term SLR in climate models is crucial for the prediction and adaptation of climate change (e.g., Oppenheimer et al. 2019; Hauer et al. 2020). Research efforts have been devoted to the evaluation of the climate models in simulating sea level climatology, sea level changes induced by anthropogenic forcing and natural climate variability, large-scale features of SLR, and related changes in ocean temperature, salinity, and atmospheric circulation (e.g., Cai et al. 2010; Bouttes et al. 2012; Pierce et al. 2012; Frankcombe et al. 2013; Lyu et al. 2020; Knutson and Ploshay 2021). For instance, Cai et al. (2010) suggested that climate models can capture the deep-reaching ocean warming in the 50°–35°S band throughout the latter half of the twentieth century that are associated with changes in surface heat flux and westerly winds over the Southern Ocean; Frankcombe et al. (2013) showed that regional sea level trends from climate model simulations are broadly consistent with satellite observation in spatial pattern for the period of 1993–2007, with enhanced regional SLR in the midlatitude band of 50°–30°S. Nevertheless, the rapid SLR within the subtropical band of 35°–20°S has received less attention, and whether climate models can faithfully represent the underlying mechanism is unknown.

The present study aims to investigate the characteristics and mechanisms of the regional SLR in the SH subtropical oceans between 35° and 20°S and evaluate its representations in climate models. By analyzing multiple observation- and model-based datasets and performing model experiments, we demonstrate that the rapid regional SLR of the SH subtropics was primarily caused by the persistent upward trend of the SAM since the mid-twentieth century. It is also found that the state-of-the-art climate models significantly underestimate the observed subtropical SLR owing to systematic biases in the simulated structure and trend magnitude of SAM. The rest of the paper is organized as follows. Section 2 describes the data and methodology. Section 3 compares the regional SLR in the SH subtropics in observation and models, explores the dynamical processes causing the SLR, and assesses the simulating biases in climate models. Section 4 summarizes the primary findings of this study and provides discussions.

2. Data and methods

a. Datasets

Five observational datasets, four ocean reanalysis products, and three ocean general circulation model (OGCM) hindcasts are utilized to characterize the sea level trends since the mid-twentieth century. The five observation-based datasets are the sea level estimate of Frederikse et al. (2020) (referred to as F20 hereinafter) for 1958–2018, the Institute of Atmospheric Physics (IAP) ocean analysis product for 1958–2017 provided by the Chinese Academy of Sciences (CAS) (Cheng et al. 2016, 2017), the World Ocean Atlas (WOA) product for 1958–2016 provided by the National Oceanic and Atmospheric Administration (NOAA)'s National Centers for Environmental Information (Levitus et al. 2012), the EN4 analysis (Good et al. 2013) for 1958–2019, and the Ishii data (Ishii et al. 2017) for 1958–2018. For F20, we use the steric sea level, which includes both thermosteric and halosteric components of the full-depth ocean but not ocean mass changes induced by changes in glaciers, ice sheets, and terrestrial water storage. For IAP, WOA, EN4, and Ishii, we analyze the steric sea level of 0–2000 m calculated using 1° × 1°, standard-level temperature, and salinity fields, which does not take into account the contribution from the deep ocean below 2000 m and ocean mass change. Steric sea level data of IAP and WOA are available for direct downloading, while EN4 and Ishii are calculated following the methods of Llovel et al. (2013) and Llovel and Lee (2015). We also computed the steric sea level of 0–700 m for comparison, which is more reliable over the historical period, and achieved similar results.

The four ocean reanalysis products are the 1° × 1° European Centre for Medium-Range Weather Forecasts (ECMWF) Ocean Reanalysis System 4 product (ORA-S4) (Balmaseda et al. 2013) for 1958–2017, the 0.25° × 0.25° ORA-S5 (Zuo et al. 2019) for 1958–2018 including the ORA-S5 backward extension for 1958–78, the 1° × 1° German contribution to the Estimating the Circulation and Climate of the Ocean project ocean synthesis version 3 (GECCO3) (Köhl 2020) for 1958–2018, and the 0.25° × 0.4° Simple Ocean Data Assimilation version 2.2.4 product (SODA2.2.4) (Giese and Ray 2011) for 1958–2010.

There are three ocean model simulations: the OGCM for the Earth Simulator (OFES) (Sasaki et al. 2008) for 1958–2017 provided by the Japan Agency for Marine-Earth Science and Technology, the Laboratory of Atmospheric Sciences and

Geophysical Fluid Dynamics (LASG)/IAP Climate Ocean Model, version 3 (LICOM3–0.1°) for 1958–2010 provided by the CAS, and LICOM3–1° for 1958–2014 provided by the CAS, as a member of phase 2 of the Ocean Model Intercomparison Project (OMIP2) (Griffies et al. 2016). LICOM3–0.1° and OFES are eddy-resolving simulations with a resolution of ~0.1°. Prior to the 1958–2010 period of our reanalysis, the two models have been integrated for 123 (65 years of spinup plus 1900–57 hindcast) and 50 (spinup) years, respectively. Yet, a model drift may still exist in the 1958–2010 output, given that eddy-resolving simulations could take a long time to stabilize. LICOM3–0.1° is forced by ECMWF Twentieth Century Reanalysis (ERA-20C) (Poli et al. 2016) for 1900–2010. LICOM3–1° is forced by the Japanese Meteorological Agency 55-year dataset for driving ocean–sea-ice models (JRA55-do; Tsujino et al. 2018), based on the JRA-55 (Kobayashi et al. 2015), and it integrates for the six cycles of the 1958–2018 period, the last cycle is used. In the model configuration, LICOM3–1° is quite similar to the CAS-LICOM3_low described in Li et al. (2020), while LICOM3–0.1° is the same as the eddy-resolving simulation of CAS-LICOM3 for OMIP2 [CAS-LICOM3_High in Li et al. (2020)]. For detailed model configurations of LICOM3–1° and LICOM3–0.1° see Lin et al. (2020) and Li et al. (2020), respectively. Because these ocean model simulations adopt volume conservation and preclude global-mean thermal expansion and ocean mass change, the sea level from LICOM3–0.1°, OFES, and LICOM3–1° is *dynamic* sea level after subtracting the global mean (e.g., Yin 2012), which is close to *regional* sea level.

The 0.25° × 0.25°, monthly satellite altimeter sea surface height data of Archiving Validation, and Interpretation of Satellite Oceanography (AVISO) (Le Traon et al. 1998) since 1993 are also used for comparison. For our analysis, all the above-mentioned datasets are resampled to 1° × 1° (without any form of prior smoothing, which may lead to aliasing of eddy variability), annual-mean sea level fields.

Four atmospheric reanalysis products are used to explore multidecadal trends in surface atmospheric conditions. They are the NOAA Twentieth Century Reanalysis version 2 (NOAA 20CR) (Compo et al. 2011) for 1958–2012, the JRA-55 product for 1958–2014, the ERA-20C product (Poli et al. 2016) for 1958–2010, and the ORA-S4 product merged of ERA-40 (Uppala et al. 2005) for 1958–88 and ERA-Interim (Dee et al. 2011) for 1989–2014. The monthly surface winds and sea level pressure (SLP) of these products are interpolated to 1° × 1° for our analysis.

b. CMIP6 and CMIP5 models

To examine the simulated SLR in climate models, we analyze historical simulations of 42 models from phase 6 of the Coupled Model Intercomparison Project (CMIP6) for 1958–2014 (Eyring et al. 2016) and 35 models from phase 5 (CMIP5) (Taylor et al. 2012) for 1958–2005. Information of these models is shown in Table 1. These historical runs are forced by the same forcing fields associated with greenhouse gases, ozone, aerosols, and solar cycle based on observation. There are subtle differences among CMIP5 and CMIP6 models numerical schemes and parameterizations, which may also contribute to the intermodel differences, in addition to internal climate variability. Note that CMIP5 and CMIP6 sea level fields are also the *dynamic* sea level.

c. Ocean model experiments

To explore mechanisms of the rapid SLR in the subtropical SIO, we perform sensitivity experiments using two ocean models, the Hybrid Coordinate Ocean Model (HYCOM) version 2.2.18 (Bleck 2002) and a 1.5-layer nonlinear reduced-gravity ocean model (RGOM). The HYCOM simulation covers the Indo-Pacific Oceans within 55°S–50°N, 19°E–68°W (Li et al. 2017; Y. Li et al. 2018). The horizontal resolution is 1/3° × 1/3° in the Indo-Pacific warm pool region (25°S–25°N, 70°–170°E) and gradually degrades to 1° × 1° in other areas, and there are 35 hybrid vertical layers. Five-degree sponge layers are applied to the northern and southern open-ocean boundaries, where the simulated temperature and salinity are relaxed to climatology. A weak sea surface salinity nudging toward monthly climatology is applied to suppress the long-term drifting of model salinity, with an *e*-folding scale of ~135 days.

After a 30-yr climatological spinup run, HYCOM is integrated forward from 1940 to 2010 under daily surface atmospheric fields of ERA-20C, which is named the Control run (HYCOM-CTRL). In HYCOM, the prescribed daily ERA-20C surface atmospheric forcing fields include surface wind stress, 10-m wind speed, shortwave, and longwave radiations, precipitation, and 2-m air temperature and humidity, while turbulent heat fluxes (latent and sensible heat fluxes) and evaporation are calculated online with model surface temperature using the Coupled Ocean–Atmosphere Response Experiment version 3.0 algorithm (Fairall et al. 2003; Kara et al. 2005). In addition to HYCOM-CTRL, two other experiments were performed for the 1940–2010 period (Table 2). The Pacific run (HYCOM-PAC) uses daily forcing in the Pacific Ocean but monthly climatologic forcing in the Indian Ocean. HYCOM-PAC is used to evaluate the impact of the Pacific Ocean climate change on the Indian Ocean through the Indonesian Throughflow (ITF). The wind stress run (HYCOM-WND) is forced with daily surface wind stress, but other forcing fields are fixed to monthly climatology. HYCOM-WND is used to evaluate the effect of wind-driven ocean dynamics on SLR. The difference between HYCOM-WND and HYCOM-PAC (i.e., HYCOM-WND minus HYCOM-PAC) roughly reflects the effect of local wind forcing on the Indian Ocean SLR, given that the Pacific winds largely control the ITF change (Li et al. 2017; Y. Li et al. 2018).

The 1.5-layer RGOM is used to simulate the first-mode baroclinic oceanic variability in response to surface wind forcing. Previous studies have shown that this model is able to capture the large-scale features of interannual and multidecadal sea level variations over the Indo-Pacific Oceans (e.g., Qiu and Chen 2012; Duan et al. 2020). In this study, we configure RGOM to the global tropical and subtropical oceans between 45°S and 45°N with horizontal resolutions of 0.25° × 0.25°. The land–sea distribution is based on the 200-m isobath of ETOPO5 bathymetry. Manual modifications are applied to the land geometry in the Indonesian seas to ensure realistic pathways of the ITF. The governing equations of the model are

TABLE 1. 42 CMIP6 and 35 CMIP5 models used in this study.

Institution	CMIP6 [typical horizontal resolution of ocean model (lon × lat)]	CMIP5 [typical horizontal resolution of ocean model (lon × lat)]
Commonwealth Scientific and Industrial Research Organisation, Australian Research Council Centre of Excellence for Climate System Science (CSIRO-ARCCSS)	ACCESS-CM2 (360 × 300) ACCESS-ESM1-5 (360 × 300)	ACCESS1.0 (360 × 300) ACCESS1.3 (360 × 300)
Alfred Wegener Institute, Helmholtz Centre for Polar and Marine Research (AWI)	AWI-CM-1-1-MR (830305)	
Beijing Climate Center (BCC)	BCC-CSM2-MR (360 × 232) BCC-ESM1 (360 × 232)	BCC-CSM1-1 (360 × 232) BCC-CSM1-1-M (360 × 232)
Chinese Academy of Sciences (CAS)	CAS-ESM2-0 (360 × 196)	
National Center for Atmospheric Research, Climate and Global Dynamics Laboratory (NCAR)	CESM2 (320 × 384) CESM2-FV2 (320 × 384) CESM2-WACCM (320 × 384) CESM2-WACCM-FV2 (320 × 384)	CCSM4 (320 × 384) CESM1-BGC (320 × 384)
Centre National de Recherches Meteorologiques; Centre Europeen de Recherche et de Formation Avancee en Calcul Scientifique (CNRM-CERFACS)	CNRM-CM6-1 (362 × 294) CNRM-ESM2-1 (362 × 294)	CNRM-CM5 (362 × 292) CNRM-CM5-2 (362 × 292)
Canadian Centre for Climate Modeling and Analysis, Environment and Climate Change Canada (CCCma)	CanESM5 (360 × 291) CanESM5-CanOE (360 × 291)	CanESM2 (256 × 192)
Centro Euro-Mediterraneo per I Cambiamenti Climatici (CMCC)		CMCC-CESM (182 × 149) CMCC-CM (182 × 149) CMCC-CMS (182 × 149)
Australian Commonwealth Scientific and Industrial Research Organization (CSIRO) Marine and Atmospheric Research in collaboration with the Queensland Climate Change Centre of Excellence (QCCCE)		CSIRO-Mk3.6.0 (192 × 189)
Lawrence Livermore National Laboratory; Argonne National Laboratory; Brookhaven National Laboratory; Los Alamos National Laboratory; Lawrence Berkeley National Laboratory; Oak Ridge National Laboratory; Pacific Northwest National Laboratory; Sandia National Laboratories (E3SM-Project)	E3SM-1-0 (360 × 180) E3SM-1-1 (360 × 180) E3SM-1-1-ECA (360 × 180)	
AEMET; BSC; CNR-ISAC; DMI; ENEA; FMI; Geomar; ICHEC; ICTP; IDL; IMAU; IPMA; KIT, Karlsruhe; KNMI; Lund University; Met Eireann; NLeSC; NTNU; Oxford University; surfSARA; SMHI; Stockholm University; Unite ASTR; University College Dublin; University of Bergen; University of Copenhagen; University of Helsinki; University of Santiago de Compostela; Uppsala University; Utrecht University; Vrije Universiteit Amsterdam; Wageningen University (EC-Earth-Consortium)	EC-Earth3 (362 × 292) EC-Earth3-Veg (362 × 292)	
The state key Laboratory of numerical modeling for Atmospheric Sciences and Geophysical fluid dynamics (LASG), Institute of Atmospheric Physics (IAP), Chinese Academy of Sciences (CAS)	FGOALS-f3-L (360 × 218) FGOALS-g3 (360 × 218)	
First Institute of Oceanography, Ministry of Natural Resources; Qingdao National Laboratory for Marine Science and Technology (FIO-QLNM)	FIO-ESM-2-0 (320 × 384)	
National Oceanic and Atmospheric Administration, Geophysical Fluid Dynamics Laboratory (NOAA-GFDL)	GFDL-CM4 (1440 × 1080) GFDL-ESM4 (720 × 576)	GFDL CM3 (360 × 200) GFDL-ESM2G (360 × 210) GFDL-ESM2M (360 × 200)
Goddard Institute for Space Studies (NASA-GISS)	GISS-E2-1-H (360 × 180)	GISS-E2-R (288 × 180) GISS-E2-R-CC (288 × 180)

TABLE 1. (*Continued*)

Institution	CMIP6 [typical horizontal resolution of ocean model (lon × lat)]	CMIP5 [typical horizontal resolution of ocean model (lon × lat)]
Met Office Hadley Centre (MOHC)	HadGEM3-GC31-LL (360 × 330) HadGEM3-GC31-MM (1440 × 1205)	HadGEM2-CC (360 × 216) HadGEM2-ES (360 × 216)
Institute for Numerical Mathematics, Russian Academy of Science (INM)	INM-CM4-8 (360 × 180) INM-CM5-0 (360 × 180)	INM-CM4 (360 × 340)
Institut Pierre Simon Laplace (IPSL)	IPSL-CM6A-LR (362 × 332)	IPSL-CM5A-LR (182 × 149) IPSL-CM5A-MR (182 × 149) IPSL-CM5B-LR (182 × 149)
Japan Agency for Marine-Earth Science and Technology; Atmosphere and Ocean Research Institute, The University of Tokyo; National Institute for Environmental Studies; RIKEN Center for Computational Science (MIROC)	MIROC-ES2L (360 × 256)	MIROC-ESM (256 × 192) MIROC-ESM-CHEM (256 × 192) MIROC4h (1280 × 912) MIROC5 (256 × 224)
Max Planck Institute for Meteorology (MPI-M)	MPI-ESM1–2-HAM (256 × 220) MPI-ESM1–2-HR (802 × 404) MPI-ESM1–2-LR (256 × 220)	MPI-ESM-LR (256 × 220) MPI-ESM-MR (182 × 149) MPI-ESM-P (256 × 220)
Meteorological Research Institute (MRI)	MRI-ESM2-0 (360 × 363)	MRI-CGCM3 (360 × 368) MRI-ESM1 (360 × 368)
Nanjing University of Information Science and Technology (NUIST)	NESM3 (362 × 292)	
Center for International Climate and Environmental Research; Norwegian Meteorological Institute; Nansen Environmental and Remote Sensing Center; Norwegian Institute for Air Research; University of Bergen; University of Oslo and Uni Research (NCC)	NorCPM1 (320 × 384) NorESM2-LM (360 × 385) NorESM2-MM (360 × 385)	NorESM1-M (320 × 384) NorESM1-ME (320 × 384)
Seoul National University (SNU)	SAM0-UNICON (320 × 384)	
Research Center for Environmental Changes, Academia Sinica (AS-RCEC)	TaiESM1 (320 × 384)	
Met Office Hadley Centre (MOHC)	UKESM1-0-LL (360 × 330)	

$$\frac{\partial u}{\partial t}+u\frac{\partial u}{\partial x}+v\frac{\partial u}{\partial y}-fv+g'\frac{\partial h}{\partial x}=A_H\nabla^2 u+\frac{\tau^x}{\rho(H+h)}, \quad (1)$$

$$\frac{\partial v}{\partial t}+u\frac{\partial v}{\partial x}+v\frac{\partial v}{\partial y}+fu+g'\frac{\partial h}{\partial y}=A_H\nabla^2 v+\frac{\tau^y}{\rho(H+h)}, \quad (2)$$

$$\frac{\partial h}{\partial t}+\frac{\partial hu}{\partial x}+\frac{\partial hv}{\partial y}=0, \quad (3)$$

where h is the upper-layer thickness (ULT) anomaly, $H = 350\,\mathrm{m}$ is the initial ULT; u and v are the zonal and meridional velocity components, respectively; f is the Coriolis parameter; $\rho = 1025\,\mathrm{kg\,m^{-3}}$ is seawater density; g' is the reduced-gravity acceleration; A_H is the coefficient of horizontal eddy viscosity, which is $2000\,\mathrm{m^2\,s^{-1}}$ between 35°S and 25°N and increases to $8000\,\mathrm{m^2\,s^{-1}}$ near model domain boundaries; and τ^x and τ^y are zonal and meridional components of surface wind stress. Within this framework, the ULT anomaly is a good proxy of dynamic sea level anomaly, and its unit is meters.

After a spinup of 20 years, the Control run (RGOM-CTRL) is performed under monthly surface winds of ERA-20C for 1958–2010. Similar to HYCOM experiments, the Pacific run (RGOM-PAC) uses monthly ERA-20C winds in the Pacific Ocean (5°S–45°N, 105°E–70°W plus 45°–5°S, 140°E–70°W) but the monthly climatological winds in the Indian and Atlantic Oceans. Similarly, in the Indian Ocean run (RGOM-IND), realistic monthly winds are used only in the Indian Ocean (5°S–45°N, 30°–105°E plus 45°–5°S, 30°–140°E), and climatological winds are used elsewhere. These two experiments can isolate the effects of Pacific and Indian Ocean winds, respectively. In addition, to examine the sensitivity to different atmospheric forcing fields, we also repeated the above experiments with winds of NOAA 20CR, ORA-S4, JRA-55, and CMIP6 ensemble mean.

d. Regional sea level trend

The sea level anomaly (SLA) discussed here is the *regional* SLA with the global-mean sea level removed. The linear trend of 1958–2014 is estimated using a least squares fitting. As such, positive and negative trends indicate faster and slower rising of regional sea level than the global mean, respectively. The ending year of 2014 is dictated by the historical simulation of CMIP6 models. The standard deviation of different observational and OGCM datasets or different model members is used to quantify the uncertainty of the ensemble-mean trend. The 95% confidence interval for the linear trend of the individual dataset is computed using an F test. Significances of linear trends and correlations are determined by the Mann–Kendall test and the two-tailed t test, respectively. The HYCOM simulation does not cover the Atlantic Ocean, and its global-mean SLR is computed by adopting ORA-S4 sea level in the Atlantic

TABLE 2. A list of the ocean model experiments analyzed in this study.

Experiment	Forcing
HYCOM-CTRL	Daily ERA-20C forcing
HYCOM-WND	Daily wind stress, other fields fixed to climatology
HYCOM-PAC	Daily forcing in Pacific, climatologic forcing in the Indian Ocean
RGOM-CTRL	Monthly wind forcing
RGOM-PAC	Monthly winds in Pacific, climatologic winds in Indian and Atlantic Oceans
RGOM-IND	Monthly winds in the Indian Ocean, climatological winds in Pacific and Atlantic

Ocean. To obtain the regional SLR of HYCOM, RGOM, and CMIP5/6 models, the global mean sea level change has been subtracted from each model.

3. Results

a. Observed and simulated SLR in the SH subtropics

We first look at the updated steric sea level reconstruction of F20. After removal of the global-mean rate of F20 steric sea level, the regional SLR over the wide latitude range of 55°–20°S is prevailingly positive in the SH during 1958–2014, with the Southern Ocean exhibiting the largest rates between 55° and 35°S (Fig. 1a). The SH subtropical oceans between 35° and 20°S, including all of the Indian, Pacific, and Atlantic sectors, show basinwide positive regional SLR rates, albeit with a few negative trends in the southeastern Pacific between 110° and 75°W which has been attributed to the boundary forcing of the South American coast (Qiu and Chen 2006). Although CMIP6 and CMIP5 models can reproduce well the largest SLR rates between 55° and 35°S, there is no evident basin-scale SLR between 35° and 20°S in the ensemble means of CMIP6 (Fig. 1b) and CMIP5 (Fig. 1c), and the underestimation is more evident in CMIP6 than in CMIP5. The robust data–model discrepancies within this latitude band demand investigation.

We further compare the zonal-mean (0°–360°E) sea level trends of F20 and CMIP6 since 1958, 1980 (the atmospheric satellite era), and 1993 (the altimeter era) (Fig. 1d). Since 1980 or 1993, ocean datasets (including observational reconstructions, ocean reanalysis products, and ocean model hindcasts) are better constrained by atmospheric and oceanic observations. The ending year of 2014 is dictated by the availability of CMIP6 historical simulations. Considering the sparsity of historical ocean observational data in the twentieth century, the zonal-average SLR may be of smaller uncertainties than the SLR rates at each grid point. CMIP6 models have underestimated the SLR between 35° and 20°S, with F20 and AVISO falling out of the one standard deviation range of 42 model members for 1980–2014 and 1993–2014, respectively; actually, the ensemble-mean trends of CMIP6 were negative for all the three periods. For 1993–2014, the F20 steric sea level trend falls in the one standard deviation range of CMIP6, which may be related to the strong internal variability during this period (Cai et al. 2019). Hereafter we focus on the 1958–2014 trend that is less influenced by internal climate variability, as indicated by the narrower intermember spread of CMIP6, and more suitable for representing the long-term SLR under climate change. In contrast, negative regional sea level trends (slower than the global-mean SLR) emerge in the tropics and subpolar North Pacific and Atlantic (Fig. 1a), which are also seen in the CMIP6 and CMIP5 models (Figs. 1b,c). During the altimeter era since 1993, strong sea level falling trends are observed in the Northern Hemisphere and the high-latitude Southern Ocean south of 55°S. CMIP6 and CMIP5 have also underestimated the regional SLR between 30° and 40°N in the Northern Hemisphere, which beyond the scope of the present study. In the following, we focus on the SLR in the SH subtropical band of 35°–20°S.

Similar to F20, other datasets (IAP, WOA, EN4, Ishii, ORA-S4, ORA-S5, GECCO3, SODA2.2.4, LICOM3–1°, OFES, and LICOM3–0.1°) all exhibit larger SLR trends in the 35°–20°S band than the global mean (Fig. 2), albeit with detailed differences in magnitude and spatial structure. Among them, SLR trends from IAP, WOA, EN4, and Ishii are relatively weaker (Figs. 2a–d) because they are steric sea level trends based on temperature and salinity of 0–2000 m without taking into account the deep-ocean contribution and ocean mass changes. In addition, the weaker SLR between 35° and 20°S of SODA2.2.4 may be related to its negative sea level trend in the Atlantic Ocean, which is different from other datasets. Note that the OGCM hindcasts are forced by atmospheric datasets (JRA-55, NCEP–NCAR, and ERA-20C for LICOM3–1°, OFES, and LICOM3–0.1°, respectively) without assimilation of ocean observational data, and they provide independent assessments of the ocean state change from observation-based datasets. Therefore, albeit with uncertainties among different products, the 12 datasets reach consensus in suggesting enhanced regional SLR in the SH subtropics.

Despite substantial interannual and decadal fluctuations, the average regional sea level of the SH subtropics shows a significant upward trend of $0.14 \pm 0.05\,\mathrm{mm\,yr^{-1}}$ for the 1958–2014 period in F20 (Fig. 3a). Relative to the $1.63 \pm 0.16\,\mathrm{mm\,yr^{-1}}$ global-mean trend for total sea level provided by F20, the SLR in the SH subtropics is faster by 8.4% ± 0.3%. The trend shows considerable sensitivity to the choice of the time period. Shifting the start time to 1980 or 1993 alters the trend values to 0.22 ± 0.10 and $0.15 \pm 0.22\,\mathrm{mm\,yr^{-1}}$, respectively. Positive trends are also obtained in other observation-based datasets (IAP, WOA, EN4, Ishii, ORA-S4, ORA-S5, GECCO3, and SODA2.2.4) and OGCM hindcasts (LICOM3–1°, OFES, and LICOM3–0.1°), the difference from the global-mean SLR rate ranges from 6.6% to 35.7% in these datasets. Based on all 12 datasets, the SLR in the SH subtropics is faster than the global-mean trend by 18.2% ± 9.9%. By contrast, ensemble-mean trends of climate models are tiny and insignificant, which are $-0.09 \pm 0.13\,\mathrm{mm\,yr^{-1}}$ for 1958–2014 in CMIP6 and $0.00 \pm 0.21\,\mathrm{mm\,yr^{-1}}$ for 1958–2005 in CMIP5, respectively (Fig. 3b). Given that assessments, predictions, and projections of climate change rely considerably on these models, these remarkable

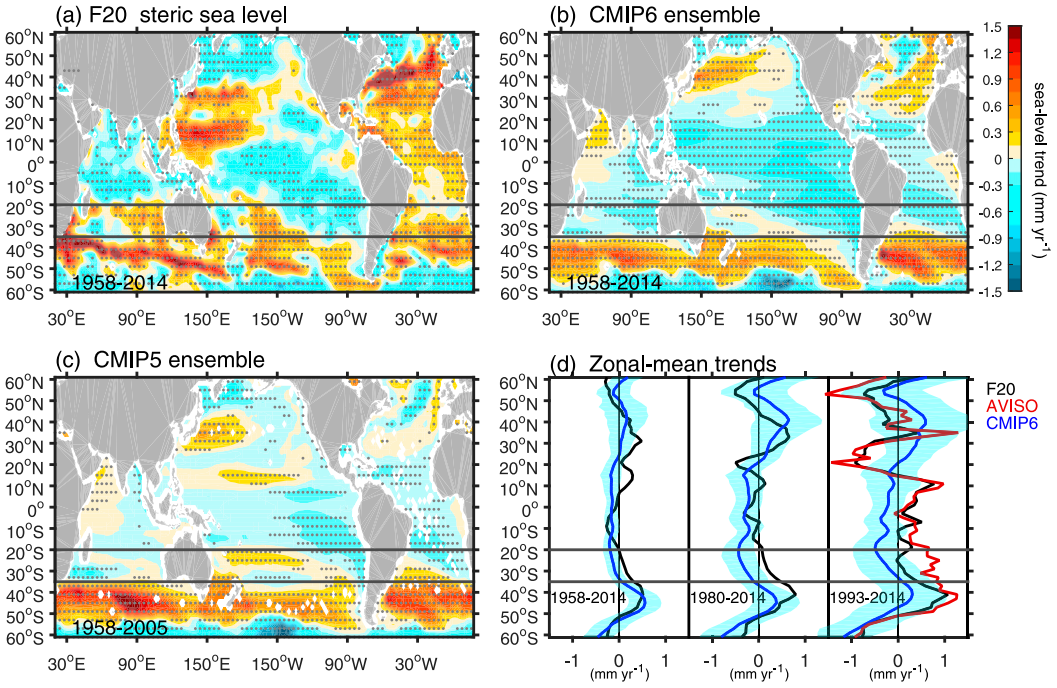

FIG. 1. Regional sea level trend patterns from observation and climate models. Linear sea level trends (mm yr^{-1}) for 1958–2014 based on (a) F20 steric sea level and (b) the ensemble mean of 42 historical simulations of CMIP6 models. (c) As in (a), but for the ensemble-mean sea level trend for 1958–2005 based on 35 historical simulations of CMIP5 models. To obtain the regional sea level, the global-mean sea level time series has been removed, such that positive (negative) trends indicate regionally faster (slower) SLR than the global mean. The black lines indicate the latitudinal range of the SH subtropics (35°–20°S). Stippling indicates significant trends at the 95% confidence level based on a Mann–Kendall test. (d) Zonal-mean (0°–360°E) sea level trends in the SH for the periods of 1958–2014, 1980–2014, and 1993–2014 derived from F20, CMIP6, and satellite altimeter data of AVISO. The global-mean sea level change has been removed from F20, CMIP6, and AVISO. The blue shading denotes one standard deviation range of 42 CMIP6 models. Note that CMIP5/6 sea level is dynamic sea level.

discrepancies are noteworthy. These discrepancies may arise from natural climate variability on decadal and interdecadal time scales (e.g., Chambers et al. 2012), which has been predominately averaged out in the CMIP5/6 ensemble mean. Alternatively, most models may contain common biases that lead to the underestimation of SLR rates over the SH subtropical oceans. Our analysis presented below supports the latter.

The simulated dynamic SLR trends from 42 CMIP6 models show a quasi-normal distribution centered at a negative value with all the nine observation-based datasets and three OGCM hindcasts plotting on its positive flank (Fig. 3c). The ORA-S5, LICOM3–0.1°, and OFES achieve stronger trends than other datasets (0.58 ± 0.10, 0.44 ± 0.08, and 0.47 ± 0.10 mm yr^{-1}; Table 3), which climate models can scarcely achieve even under extreme scenarios of natural variability. The model drift due to insufficient spinup may contribute to the strong SLR in LICOM3–0.1° and OFES, and the usage of ORA-S5 backward extension for 1958–78 may enhance SLR in ORA-S5. A comparison with AVISO satellite data suggests that ORA-S5, LICOM3–0.1°, and OFES show realistic SLR rates since 1993 without significant overestimation (Fig. 4). The data–model contrasts are discernible in all of the southern Indian Ocean (35°–20°S, 50°–110°E), Pacific (35°–20°S, 150°E–130°W), and Atlantic (35°–20°S, 40°W–0°) basins (Figs. 3d–f), over which the 12 datasets show mean trends of 0.48 ± 0.32, 0.40 ± 0.19, and 0.36 ± 0.28 mm yr^{-1} versus ensemble-mean trends of −0.11 ± 0.23, 0.01 ± 0.24, and −0.05 ± 0.24 mm yr^{-1} from CMIP6 models. Among the three ocean basins, the SIO shows the largest data–model contrast in the ensemble-mean sense (0.48 vs −0.11 mm yr^{-1}), and its sea level dynamics is subjected to a larger degree of complexity owing to the strong modulation effect from the Pacific via the ITF (e.g., Jyoti et al. 2019; Sprintall et al. 2014; Schwarzkopf and Böning 2011). Hereafter we adopt the SIO as an example to explore the mechanisms responsible for the enhanced SLR in the SH subtropics without the loss of generality for the three ocean basins. Worthy of note is that data–model differences in three basins are all statistically significant at the 95% confidence level based on the *t* test, with *p* values of 0.004, 0.015, and 0.028 for SIO, southern Pacific Ocean, and the southern Atlantic Ocean, respectively.

b. *Causes for the SLR*

Several recent studies have explored the long-term regional SLR in the southern Pacific and Atlantic Oceans (e.g., Vianna

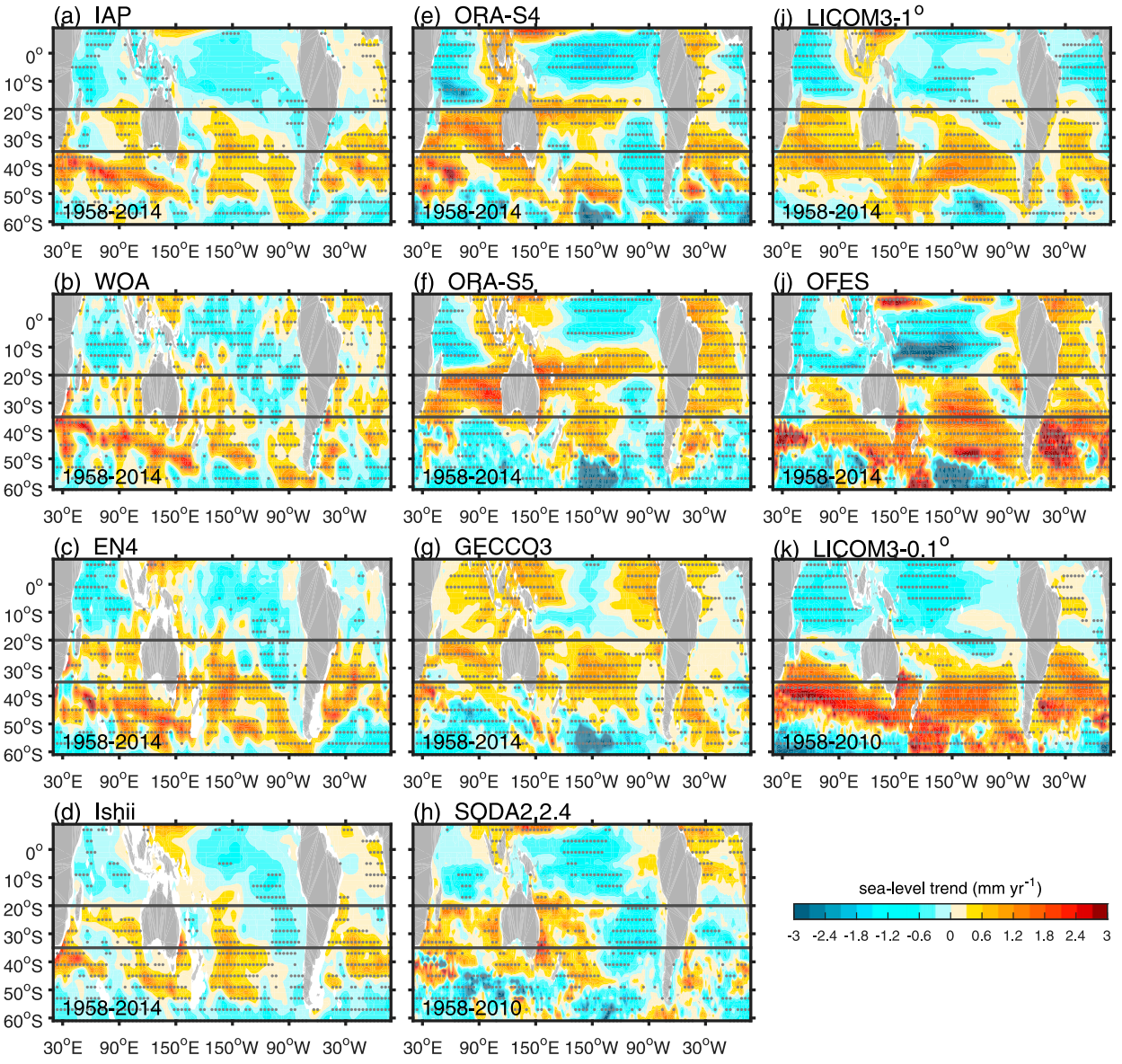

FIG. 2. Regional sea level trends of the SH in observation-based datasets and OGCM hindcasts. Linear sea level trends (mm yr^{-1}) for 1958–2014 derived from (a) IAP, (b) WOA, (c) EN4, (d) Ishii, (e) ORA-S4, (f) ORA-S5, (g) GECCO3, (i) LICOM3–1°, and (j) OFES. (h),(k) As in (a), but for 1958–2010 based on SODA2.2.4 and LICOM3–0.1°, respectively. The global-mean SLR has been removed. The black lines indicate the latitudinal range of the SH subtropics (35°–20°S). Stippling indicates significance at the 95% confidence level based on a Mann–Kendall test.

and Menezes 2013; Roemmich et al. 2015, 2016; Llovel and Terray 2016; Volkov et al. 2017; Frederikse et al. 2021), while the mechanism for SLR in the SIO has not been firmly established. Existing studies have emphasized the essential role played by the ITF in driving the overall sea level changes in the SIO on decadal and longer time scales (e.g., Jyoti et al. 2019; Sprintall et al. 2014; Schwarzkopf and Böning 2011), while there are other studies suggesting the importance of local wind forcing in determining the SLR pattern (e.g., Lee and McPhaden 2008; Han et al. 2010; Li and Han 2015; Volkov et al. 2020). To evaluate the relative importance of these two processes, we perform sensitivity experiments using the HYCOM and the 1.5-layer RGOM.

The control runs of the two models, HYCOM-CTRL and RGOM-CTRL, robustly capture the rapid SLR in the SIO over 1958–2010 (Fig. 5). As referenced to F20, the control runs show realistic evolutions of the sea level in the SIO (Fig. 5a). The correlations of HYCOM-CTRL and RGOM-CTRL with F20 are 0.59 and 0.47, respectively. HYCOM-WND, which retains only the surface wind stress variability while fixing the other forcing fields (e.g., heat and freshwater fluxes) to climatology, produces results rather close to those of HYCOM-

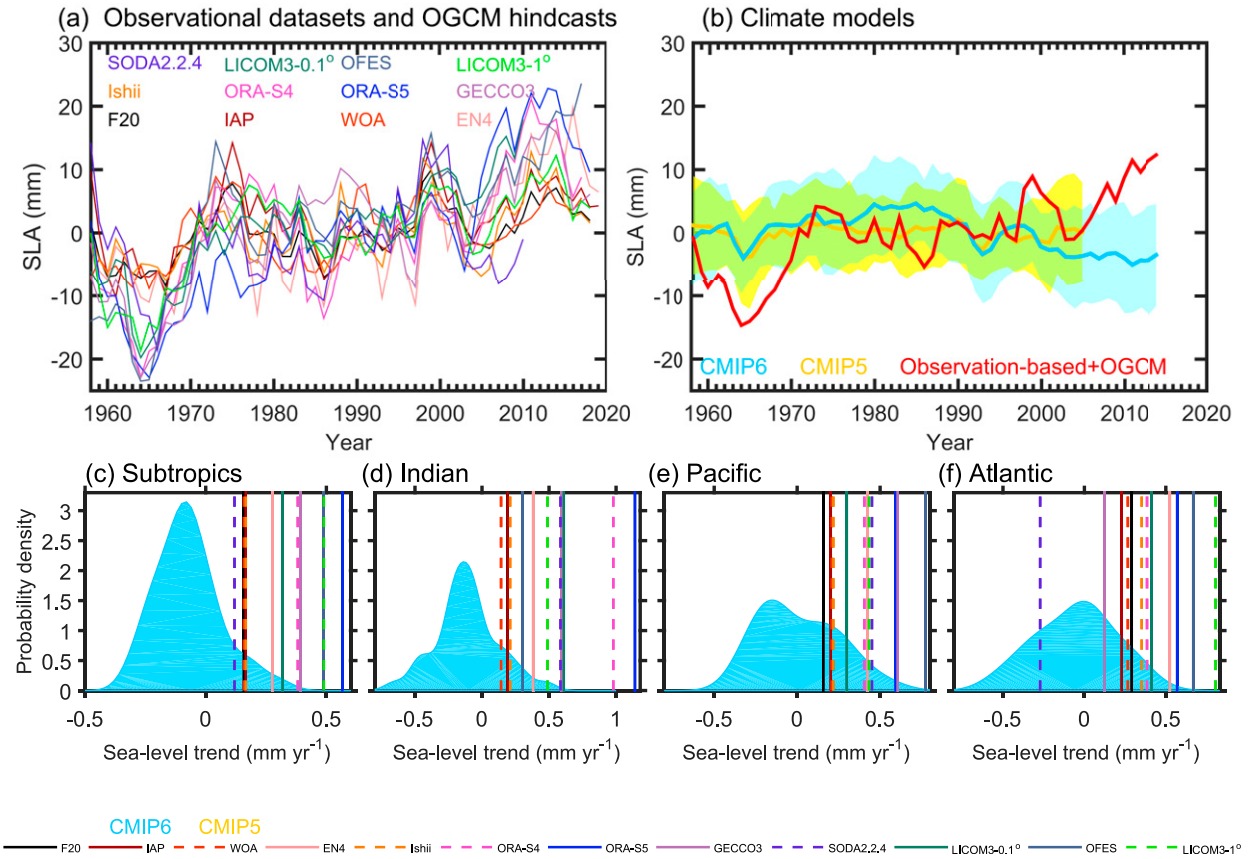

FIG. 3. SH subtropical (35°–20°S) sea level changes from observation-based datasets, OGCM hindcasts, and climate models. Annual sea level anomalies (SLAs) averaged over the SH subtropics (35°–20°S) derived from (a) the nine observation-based datasets (F20, IAP, WOA, Ishii, EN4, ORA-S4, ORA-S5, GECCO3, and SODA2.2.4) and three OGCM hindcasts (LICOM3–0.1°, OFES, and LICOM3–1°) since 1958 and from (b) historical simulations of CMIP6 models (blue) for 1958–2014 and CMIP5 models (yellow) for 1958–2005. The ensemble-mean SLA of 12 datasets for 1958–2014 is also shown in (b). Shadings show the standard deviation ranges of climate models. Probability density distributions of the 1958–2014 sea level trends for (c) the subtropics of the SH, (d) the southern Indian Ocean (SIO; 35°–20°S, 50°–110°E), (e) the southern Pacific Ocean (35°–20°S, 150°E–130°W), and (f) the southern Atlantic Ocean (35°–20°S, 40°W–0°) derived from CMIP6 simulations. SLR derived from the nine observation-based datasets and three OGCM hindcasts can be obtained from Table 3.

CTRL (Figs. 5a–c), confirming the dominance of surface wind forcing in driving the regional SLR. HYCOM-PAC, which uses time-varying winds in the Pacific Ocean and climatologic winds in the Indian Ocean, cannot reproduce the observed changes (Fig. 5d), yielding a sea level falling of $-0.06 \pm 0.21\,\mathrm{mm\,yr^{-1}}$ in the SIO (i.e., slower than the global mean). This result eliminates the ITF as the primary driver of the SLR in the SIO. The difference between HYCOM-WND and HYCOM-PAC (i.e., HYCOM-WND minus HYCOM-PAC) can represent the forcing effect of local winds in the Indian Ocean. It shows an SLR rate of $0.76 \pm 0.23\,\mathrm{mm\,yr^{-1}}$ in the SIO (Fig. 5e), implying the dominance of the local wind forcing. HYCOM results are confirmed by RGOM experiments. The RGOM-PAC and RGOM-IND runs forced by time-varying Pacific and Indian Ocean winds simulate ULT trends of 0.01 ± 0.02 and $0.21 \pm 0.03\,\mathrm{m\,yr^{-1}}$ in the SIO, respectively (Figs. 5g,h). We also repeated the RGOM experiments using three other atmospheric datasets (NOAA 20CR, ORA-S4, and JRA-55) as the forcing fields, and results are consistent with those forced by ERA-20C in suggesting the dominance of local winds in causing the SLR in the SIO (Figs. 6a–f). These results underpin the importance of local wind forcing within the Indian Ocean in driving the regional SLR.

Note that some regions show considerable sensitivity to the choice of wind forcing, particularly in the South Pacific. Although coarse-resolution models are not able to fully represent the complicated ITF pathways and variabilities, the control runs of HYCOM and RGOM can, to some extent, capture the ITF transport variability on interannual-to-interdecadal variations (figures not shown), showing a variability amplitude of ~ 5 Sv ($1\,\mathrm{Sv} \equiv 10^6\,\mathrm{m^3\,s^{-1}}$), and correlated with ENSO. The modeled ITF also shows a strengthening trend since the early 1990s. These changes in model simulations are generally consistent with observation-based ITF studies estimates (e.g., Meyers 1996; Sprintall et al. 2009; Sprintall and Révelard 2014; Liu et al. 2015; Susanto and Song 2015).

TABLE 3. Regional SLR (mm yr^{-1}) derived from nine observation-based datasets and three OGCM hindcasts. An asterisk indicates insignificance at the 95% confidence level based on the two-tailed *t* test. Note that trends from SODA2.2.4 and LICOM3–0.1° are for the 1958–2010 period.

Region	F20	IAP	WOA	EN4	Ishii	ORA-S4	ORA-S5	GECCO3	SODA2.2.4	LICOM3–0.1°	OFES	LICOM3–1°
Subtropics	0.14 ± 0.05	0.15 ± 0.08	0.13 ± 0.07	0.27 ± 0.08	0.15 ± 0.06	0.39 ± 0.11	0.58 ± 0.09	0.42 ± 0.09	0.11 ± 0.11	0.44 ± 0.07	0.47 ± 0.09	0.30 ± 0.08
Indian	0.19 ± 0.15	0.19 ± 0.19	0.14 ± 0.19*	0.38 ± 0.21	0.21 ± 0.17	0.98 ± 0.22	1.14 ± 0.18	0.59 ± 0.23	0.59 ± 0.21	0.49 ± 0.22	0.30 ± 0.16	0.61 ± 0.15
Pacific	0.16 ± 0.16	0.20 ± 0.19	0.21 ± 0.17	0.42 ± 0.24	0.22 ± 0.19	0.41 ± 0.22	0.59 ± 0.19	0.61 ± 0.21	0.45 ± 0.29	0.43 ± 0.19	0.77 ± 0.27	0.30 ± 0.21
Atlantic	0.29 ± 0.10	0.23 ± 0.16	0.27 ± 0.17	0.53 ± 0.16	0.35 ± 0.12	0.38 ± 0.12	0.57 ± 0.18	0.12 ± 0.14*	−0.27 ± 0.17	0.81 ± 0.17	0.67 ± 0.14	0.41 ± 0.18

Given the dominance of local wind forcing, we next explore changes in surface atmospheric circulation. The ERA-20C reanalysis, as the forcing fields for LICOM3–0.1°, HYCOM, and RGOM, exhibits anticyclonic (counterclockwise) surface wind trends over the SIO during 1958–2010, with southeasterly trends over 30°–10°S and northwesterly trends south of 40°S (Fig. 7a). Anticyclonic winds favor upper-ocean convergence through downward Ekman pumping (Han et al. 2010), which is largely responsible for the rapid SLR in the SIO. These wind trends correspond to a strengthening of the Mascarene high (Xue et al. 2003) that manifests as positive SLP trends in the SIO. Actually, the three subtropical highs in the SH were all strengthened, accompanied by anticyclonic wind trends in all the SH ocean basins. These features, along with the circumpolar westerly winds in the Southern Ocean, greatly resemble the positive phase of SAM. Similar wind and SLP trend patterns are seen in three other atmospheric reanalyses (Figs. 7b–d).

By calculating the SAM index and Mascarene high intensity, we further evaluate their relationship. Among them, the SAM index is calculated as the zonal-mean SLP difference between 40° and 65°S (Gong and Wang 1998), and the Mascarene high intensity is defined as the SLP anomaly averaged over the region of 35°–20°S, 50°–110°E. As shown in Fig. 8, the trends of Mascarene high intensity and SAM bear correspondence among four atmospheric datasets, with significant instantaneous correlations of 0.51, 0.39, 0.32, and 0.50 for ERA-20C, NOAA 20CR, ORA-S4, and JRA-55, respectively. In addition, we have also checked the relationship between the SAM and the SLP difference between the Mascarene high and its poleward neighboring region (70°–50°S, 50°–110°E), and significant instantaneous correlations of 0.74, 0.69, 0.59, and 0.72 for ERA-20C, NOAA 20CR, ORA-S4, and JRA-55, respectively, are found. The long-term correlation implies the importance of SAM in driving the atmospheric and oceanic changes in the SH subtropics, as speculated by a few recent studies (e.g., Qu et al. 2019; Roemmich et al. 2016; Yang et al. 2020).

In addition to the influence of the Southern Ocean climate, the Mascarene high changes may also originate from the tropics (Lau and Kim 2015). In particular, the persistent warming of the tropical Indian Ocean (TIO) (e.g., Roxy et al. 2014; Du and Xie 2008) may have enhanced the local SLP depression and thereby strengthened the Indian Ocean Hadley cell (Han et al. 2010) along with its descending branch—the Mascarene high. Given this, we next estimate the potential impacts from the TIO. Following Nguyen et al. (2013), we define the Hadley cell intensity of the SIO as the vertically averaged maximum value of zonal-mean meridional mass streamfunction between 900 and 200 hPa. The mass streamfunction is defined as

$$\psi(P,y) = \frac{2\pi R\cos(y)}{g}\int_{P}^{P_s} V(P,y)\,dP, \tag{4}$$

where V is the 40°–110°E mean meridional component of the total wind, R is the average radius of Earth, g is the gravitational acceleration, y latitude, P is pressure, and P_S is surface pressure. For the TIO low-pressure intensity, the SLP anomaly

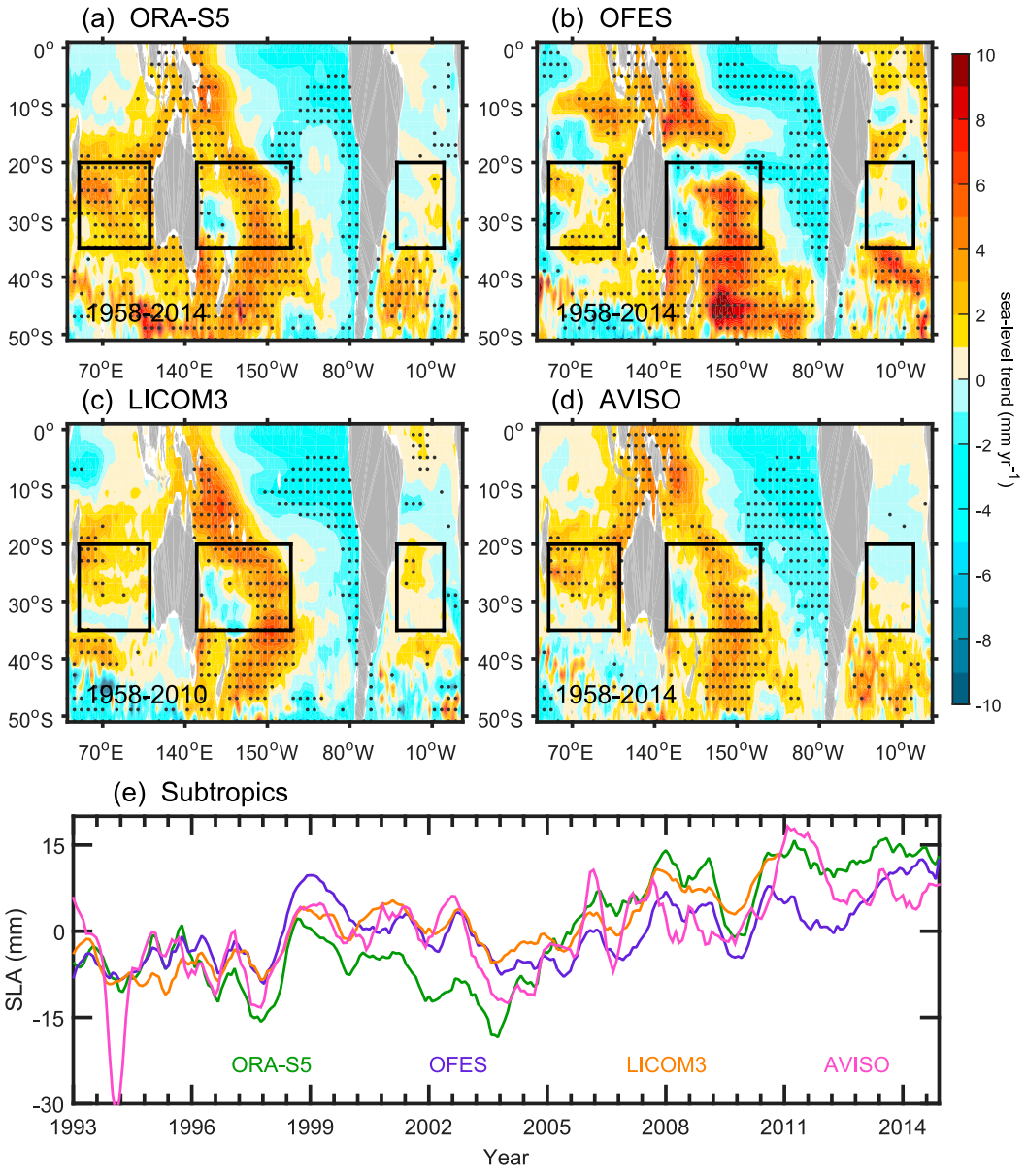

FIG. 4. Sea level trends in OGCM hindcasts and AVISO satellite observation. Linear sea level trends (mm yr^{-1}) derived from (a) ORA-S5 for 1993–2014, (b) OFES for 1993–2014, (c) LICOM3–0.1° for 1993–2010, and (d) AVISO for 1993–2014. The global-mean SLR has been removed. Stippling indicates significance at the 95% confidence level based on a Mann–Kendall test. Three boxes denote the SIO (35°–20°S, 50°–110°E), southern Pacific Ocean (35°–20°S, 150°E–130°W), and southern Atlantic Ocean (35°–20°S, 40°W–0°). (e) Monthly SLAs (in mm) averaged over the SH subtropics (35°–20°S) derived from the ORA-S5, OFES, LICOM3–0.1°, and AVISO. All variables are smoothed with a 6-month window to reduce the seasonal cycle effect.

averaged over the 20°S–20°N, 40°–110°E is used as a proxy. However, since the SLP depression was weakened in three out of four atmospheric datasets, and the trend of Hadley cell intensity is hard to determine (e.g., Mitas 2005) (Fig. 7e), an evident forcing effect from the tropical climate seems unlikely. By contrast, the SAM and the Mascarene high exhibit robust positive trends, and a stronger trend in the former generally warrants a stronger trend in the latter. Linear regression analysis also suggests that the SAM-induced SLP anomalies are stronger than those associated with TIO change in the SH subtropics and greatly resemble the observed SLP trends in spatial structure (Fig. 9). Overall, the SAM represents the primary driver of surface atmospheric changes over the SIO, while the influence from the TIO seems weak.

c. *Biases in climate models*

We then turn our focus to climate model simulations. CMIP6 models produce very weak surface atmospheric changes in the

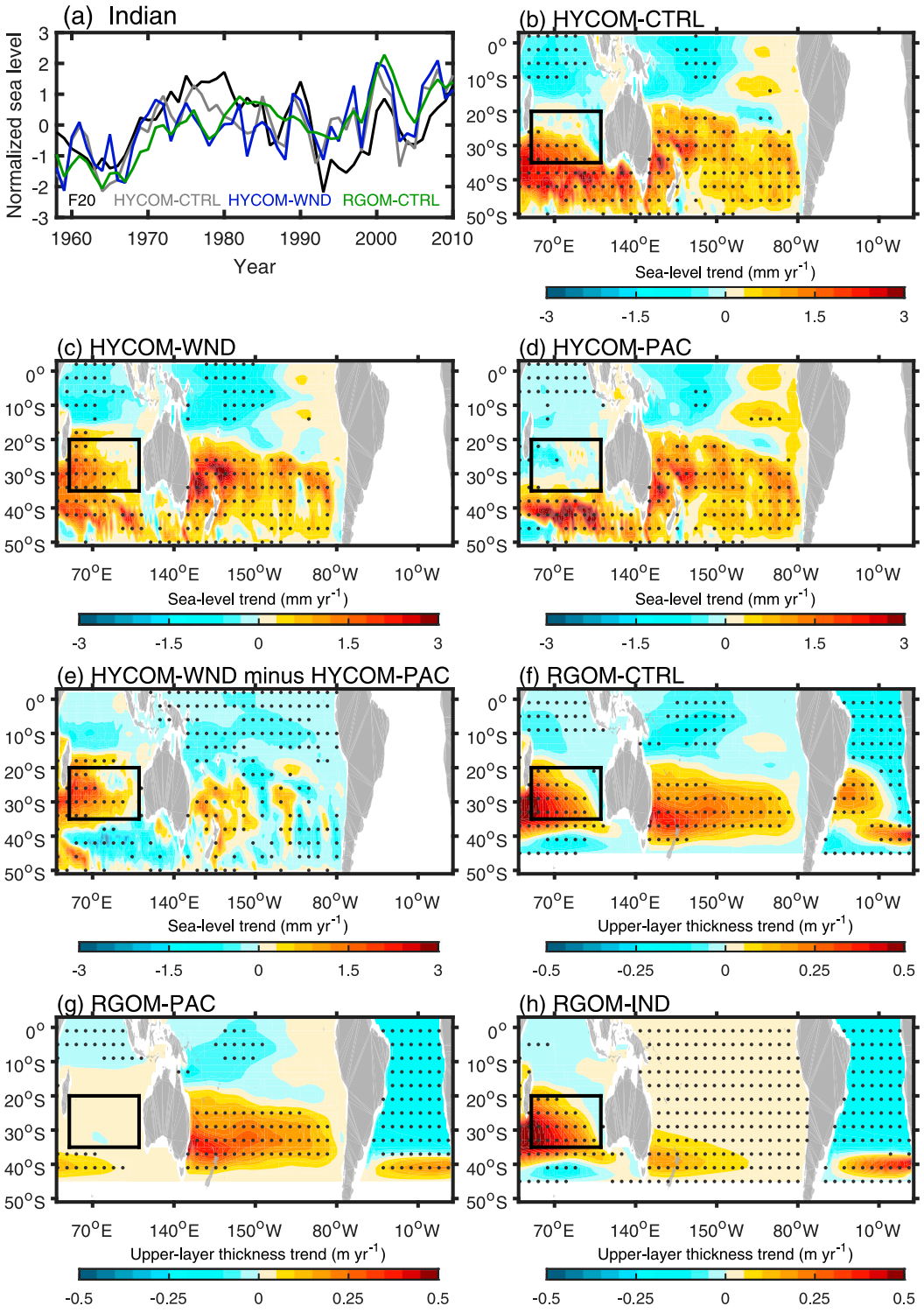

FIG. 5. Effects of surface wind forcing on SLR in the SIO. (a) Annual SLAs and the ULT anomaly averaged over the subtropical SIO derived from F20, HYCOM-CTRL, HYCOM-WND, and RGOM-CTRL. All variables are normalized by their standard deviations. Linear sea level trends (mm yr^{-1}) for 1958–2010 derived from (b) HYCOM-CTRL, (c) HYCOM-WND, (d) HYCOM-PAC, and (e) HYCOM-WND minus HYCOM-PAC. (f)–(h) As in (b), (d), and (e), but for the ULT trends (m yr^{-1}) derived from (f) RGOM-CTRL, (g) RGOM-PAC, and (h) RGOM-IND. The global-mean SLR has been removed. The black box denotes the SIO (35°–20°S, 50°–110°E). Stippling indicates significance at the 95% confidence level.

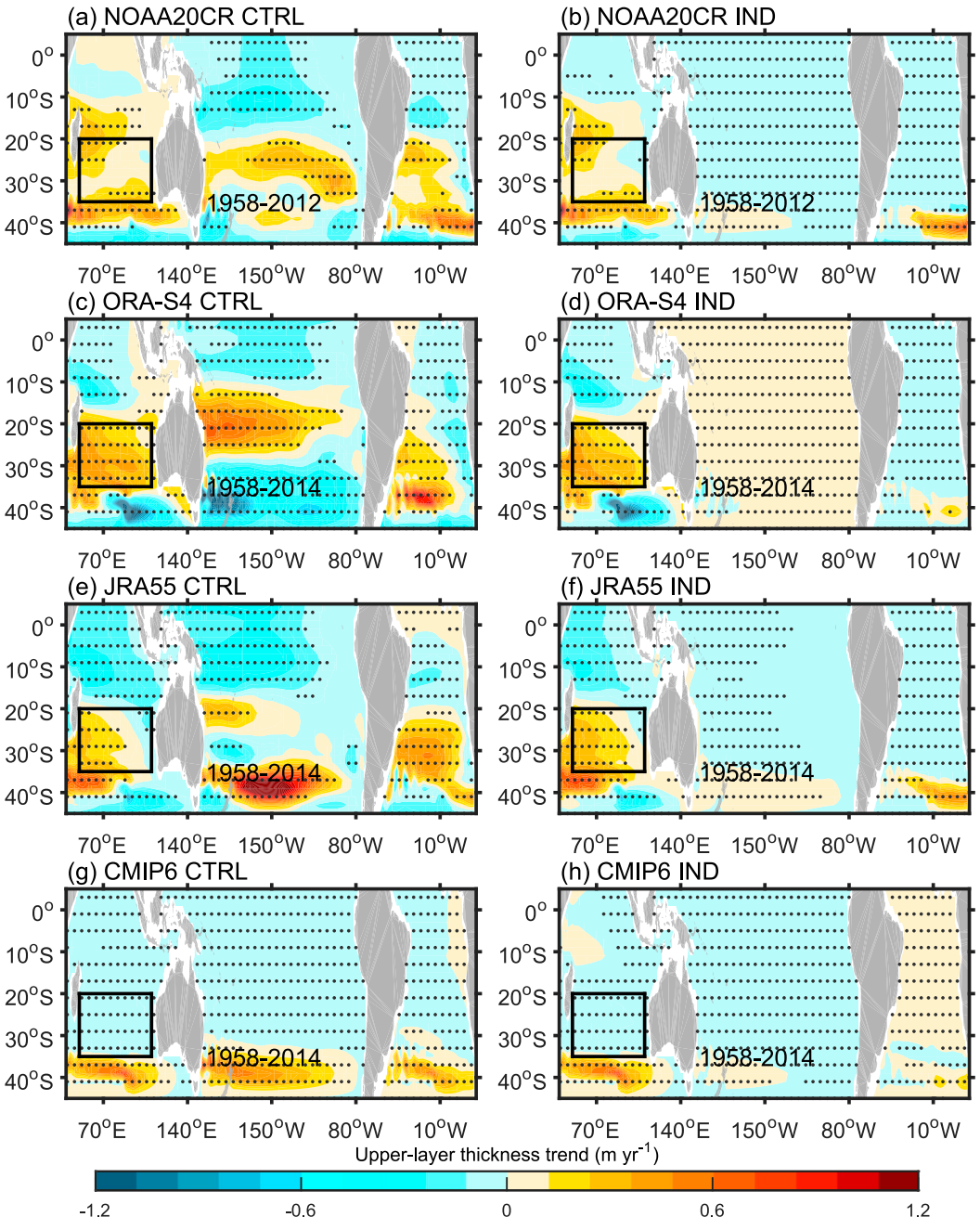

FIG. 6. Ocean response to different atmospheric datasets in the 1.5-layer RGOM. Linear ULT trends (m yr^{-1}) derived from (a) CTRL and (b) IND runs forced by NOAA 20CR winds for 1958–2012. Other panels are as in (a) and (b), but forced by (c),(d) ORA-S4 winds, (e),(f) JRA-55 winds, and (g),(h) CMIP6 ensemble-mean winds for 1958–2014. Stippling indicates significance at the 95% confidence level based on a Mann–Kendall test.

SIO, and the SAM-related positive SLP trends are basically confined to the Southern Ocean south of 35°S (Fig. 10a). Most models obviously underestimate the observed enhancement of the Mascarene high (Fig. 10b); the trends of three of the atmospheric datasets fall entirely out of the climate model spread, and the average trend (2.03 ± 1.03 Pa yr^{-1}) of the four atmospheric datasets exceeds all members. Meanwhile, although climate models also show positive trends in SAM, the magnitudes are generally weaker than in observation (Fig. 10c). The SAM-related SLP trends in observation vary from negative to positive at ~45°S, with the maximum positive trend at ~40°S (Fig. 10d). Model simulations produce broadly similar SLP trends, but the maximum trend is shifted southward as compared to reanalysis products. As quantified by

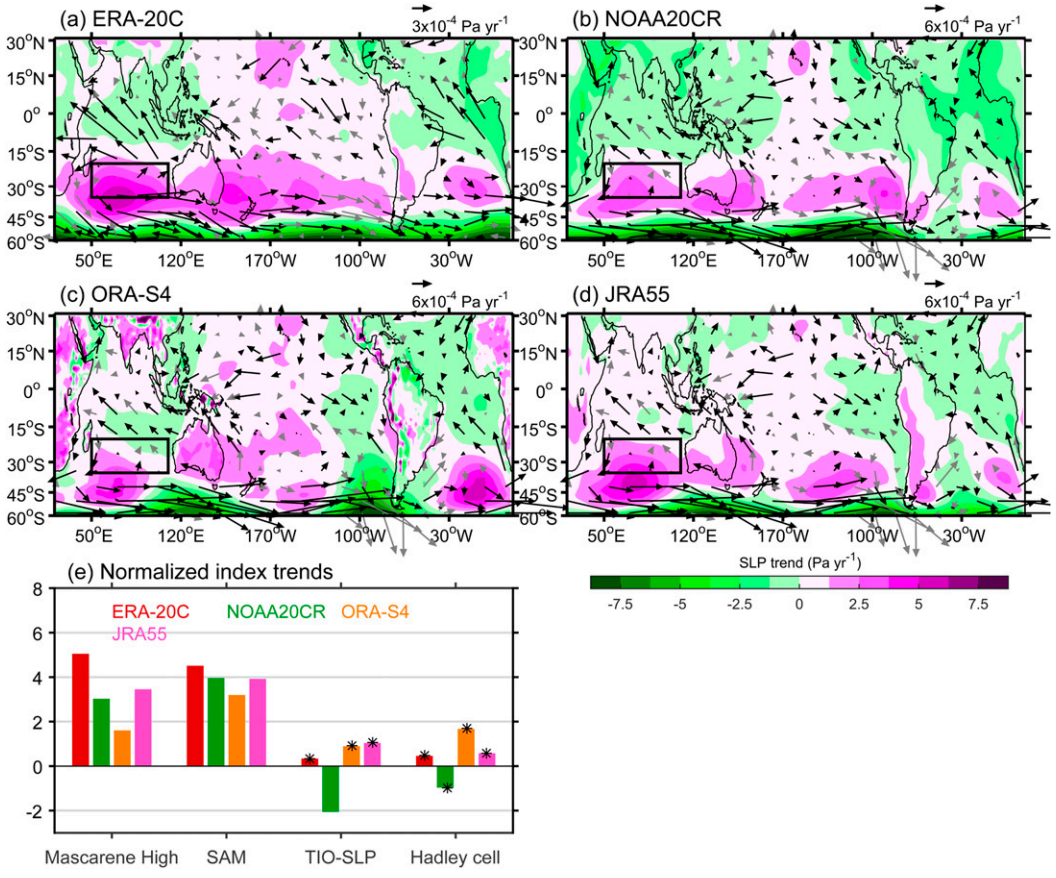

FIG. 7. Changes of surface atmospheric circulation in atmospheric datasets. Linear trends of the sea level pressure (SLP; color shading; in Pa yr^{-1}) and wind stress (arrows; in Pa yr^{-1}) derived from (a) ERA-20C for 1958–2010, (b) NOAA 20CR for 1958–2012, (c) ORA-S4 for 1958–2014, and (d) JRA-55 for 1958–2014. Zonal wind stress trends below the 90% confidence level are plotted as gray arrows, and the values on land are not shown. (e) Trends of the Mascarene high intensity, SAM index, tropical Indian Ocean SLP (TIO-SLP), and Hadley cell intensity derived from the four atmospheric datasets (ERA-20C for 1958–2010, NOAA 20CR for 1958–2012, ORA-S4 for 1958–2014, and JRA-55 for 1958–2014). The ORA-S4 product is the combination of ERA-40 for 1958–88 and the ERA-Interim for 1989–2014. Asterisks denote below the 95% confidence level. All trends are normalized by the standard deviation.

the maximum trend of the ensemble-mean SLP, this mismatch is as large as ~8°. Despite considerable differences among atmospheric reanalysis products, the ensemble-mean SLP of CMIP6 is shifted to the south as referenced to any of the four reanalysis products. As such, climate models produce the opposite scenarios to observation; that is, models tend to generate easterly wind trends near 35°S on the northern flank of the positive SLP maximum (Fig. 10a), and cyclonic wind trends act to hinder the subtropical SLR. This explains the negative regional sea level trend (slower than the global-mean SLR) in the CMIP6 ensemble-mean (-0.11 mm yr^{-1}; Fig. 3d). We also performed RGOM experiments using CMIP6 ensemble winds (Figs. 6g,h), and the results confirm that the CMIP6 winds cannot give rise to enhanced SLR in the SH subtropics. Similarly, CMIP5 models also show systematic biases in simulating the trends of SAM and its SLP signatures (figures not shown). These biases in the simulated atmospheric changes likely lead to the missing SLR features in the SH subtropical oceans.

The persistent upward trend of SAM has been attributed primarily to the stratospheric ozone depletion over the Antarctic (e.g., Cai and Cowan 2007; Thompson et al. 2011) and secondary to greenhouse gas forcing (e.g., Swart and Fyfe 2012). Yet, present climate models are unable to accurately take into account the effect of ozone loss; some models use prescribed monthly, zonally symmetric ozone concentrations (e.g., Eyring et al. 2013, 2016). It has been suggested that models without interactive atmospheric chemistry tend to severely underestimate the magnitude of ozone variability and its impact on atmospheric circulation (e.g., Neely et al. 2014; Waugh et al. 2009). Also, the chemistry models have shown biases in reproducing the observed ozone concentration (Stevenson et al. 2013). In addition, considerable model biases exist in the climatology of the high-latitude surface–atmosphere flux

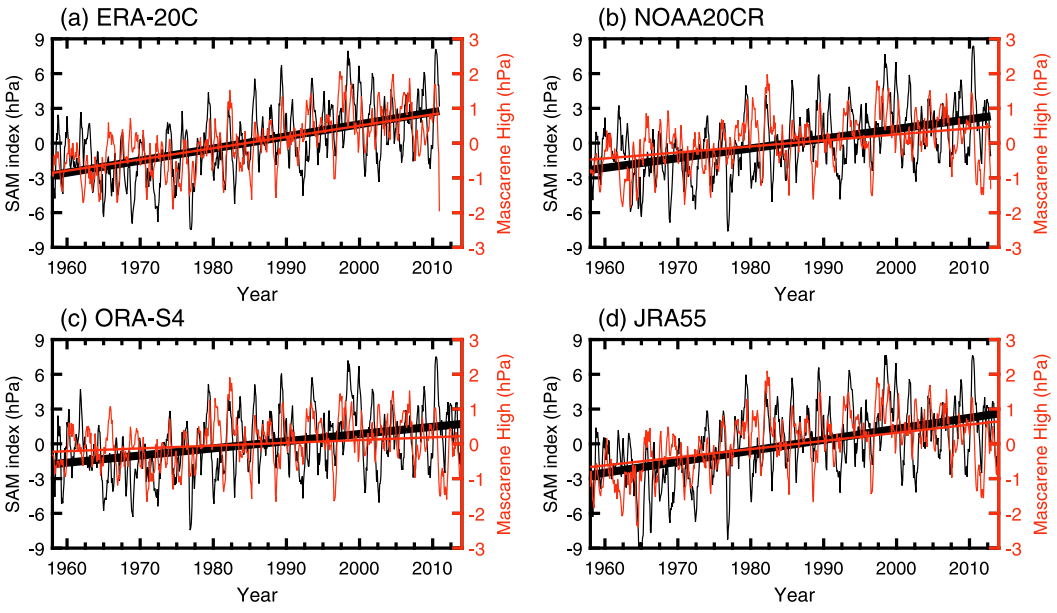

FIG. 8. SAM and Mascarene high in atmospheric datasets. Monthly SAM index (hPa) and Mascarene high intensity anomaly (hPa) derived from (a) ERA-20C for 1958–2010, (b) NOAA 20CR for 1958–2012, (c) ORA-S4 for 1958–2014, and (d) JRA-55 for 1958–2014, with a 6-month smoothing to reduce the effect of the seasonal cycle. Straight lines denote their linear trends based on the least squares fitting.

(Hwang and Frierson 2013), possibly linked to the surface warming bias in the Southern Ocean (Wang et al. 2014). All the deficiencies likely contribute to the weaker (Fig. 10b) and southward-shifted SLP trends associated with SAM in models (Fig. 10d).

Owing to natural climate variability, a few models replicate the SLR in the SIO with adequate magnitudes (Fig. 3d). However, these SLR trends are not driven by local atmospheric changes as reality; the SLR does not show cross-member correspondence with the SAM change (Fig. 10e). Rather, they are largely forced remotely by the Pacific Walker circulation, as evidenced by the significant negative cross-member correlation between the Pacific Walker circulation proxy and the SIO SLR (Fig. 10f). Enhancement of the Pacific Walker circulation arising from natural climate variability can cause the SIO SLR by strengthening the ITF transport—a mechanism operating on the decadal time scale (Jyoti et al. 2019). Yet, the Pacific Walker circulation was not enhanced but instead slightly weakened over the central and eastern Pacific basin since the mid-twentieth century (e.g., Tokinaga et al. 2012; Vecchi et al. 2006) according to atmospheric datasets (Figs. 7a–d), and there is no observational evidence to suggest a persistent enhancement of the ITF transport since the mid-twentieth century (e.g., M. Li et al. 2018). There is a negative correlation (−0.49) between the SLR and the Mascarene high intensity in CMIP6 (Fig. 10g), which is contrary to the observed relationship. Since the SAM-related subtropical atmospheric changes are too weak in models to dictate the SIO sea level change (Figs. 10b,d), the tropical Pacific forcing becomes dominant. Therefore, although some model members parallel the observation, the underlying mechanisms differ due to systematic biases in the simulated SAM.

4. Summary and discussion

Decadal and interdecadal sea level changes over the SH subtropical oceans between 35° and 20°S have been reported, but the long-term SLR since the 1950s in this latitude band has not fully comprehended, which most state-of-the-art climate models have significantly underestimated. Our work reveals the critical impacts of the human-induced Southern Ocean climate on the rapid SH subtropical SLR and links the failure of climate models in reproducing observed SLR to the underestimation of the SAM trend and the bias in SAM trend position, highlighting the urgency for improving the model simulation of the SH climate.

Observation-based and OGCM datasets reveal that the SLR of the SH subtropics (35°–20°S) is faster than the global mean rate by 18.2% ± 9.9% for the 1958–2014 period. This rapid SLR is primarily attributable to the persistent upward trend of the SAM, while the influence of tropical climate variability is minimal in the SIO. The upward trend of SAM gave rise to enhancements of the subtropical highs in the SH, which is favorable for regional SLR by driving upper-ocean convergence. Systematic biases are detected in the simulated structure and trend magnitude of the SAM in climate models, with a robust underestimation of the SAM's signatures in the SH subtropics. These systematic biases of climate models are the key to the underestimated SLR. As a result, climate models are not able to correctly simulate the observed SLR between 35° and 20°S.

The intermodel spread of CMIP6 is used to assess the influence of internal variability. Our results show that few

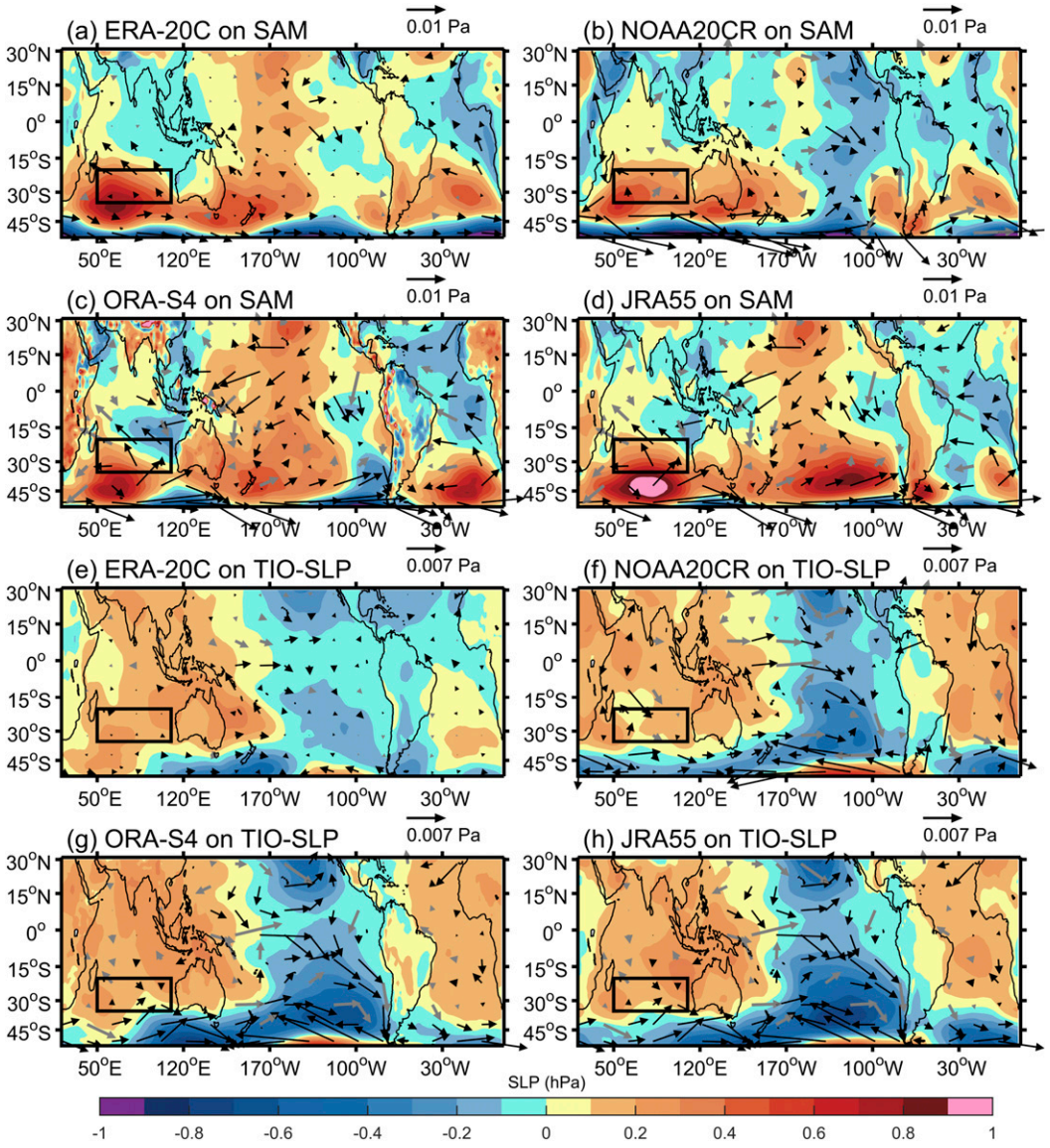

FIG. 9. Multiple linear regressions of SLP and wind stress on the SAM and TIO-SLP. Multiple linear regression of SLP (color shading; in hPa) and wind stress (arrows; in Pa) anomalies on the SAM index derived from (a) ERA-20C for 1958–2010, (b) NOAA 20CR for 1958–2012, (c) ORA-S4 for 1958–2014, and (d) JRA-55 for 1958–2014. (e)–(h) As in (a)–(d), but regressed on the TIO-SLP index. Zonal wind stress trends below the 90% confidence level based on an F test are plotted as gray arrows, and the values on land are not shown. An 8-yr low-pass Hanning filter is applied to anomaly fields and indices to reduce the interannual variability effect.

CMIP6 models can reach the SLR rates in the SIO as in observational datasets such as F20, IAP, WOA, EN4, and Ishii (Fig. 3d), and the Mascarene high trends from three atmospheric reanalyses fall out of the range of the 42 CMIP6 members (Fig. 10b). Considering that the spread of CMIP6 still contains the effect of the difference in model configurations, we also analyzed the large ensemble simulations of the NCAR Community Earth System Model version 1 (CESM-LE) (Hurrell et al. 2013; Kay et al. 2015) and obtained similar results (figures not shown). CESM-LE has 40 ensemble members with the same model configuration and same external forcing. As such, the intermember difference arises merely from internal climate variability. These comparisons indicate that the trends in the SIO cannot be explained by internal climate variability.

Although mechanisms of the SLR and origins of model errors are established in the SIO, the understanding may also apply to the South Pacific and Atlantic. We performed similar RGO experiments to those of Fig. 5 and found that the regional SLR trends in the South Pacific and Atlantic Oceans were also driven by local forcing of subtropical highs (figures not shown). Yet, the specific mechanisms working in the South Pacific and

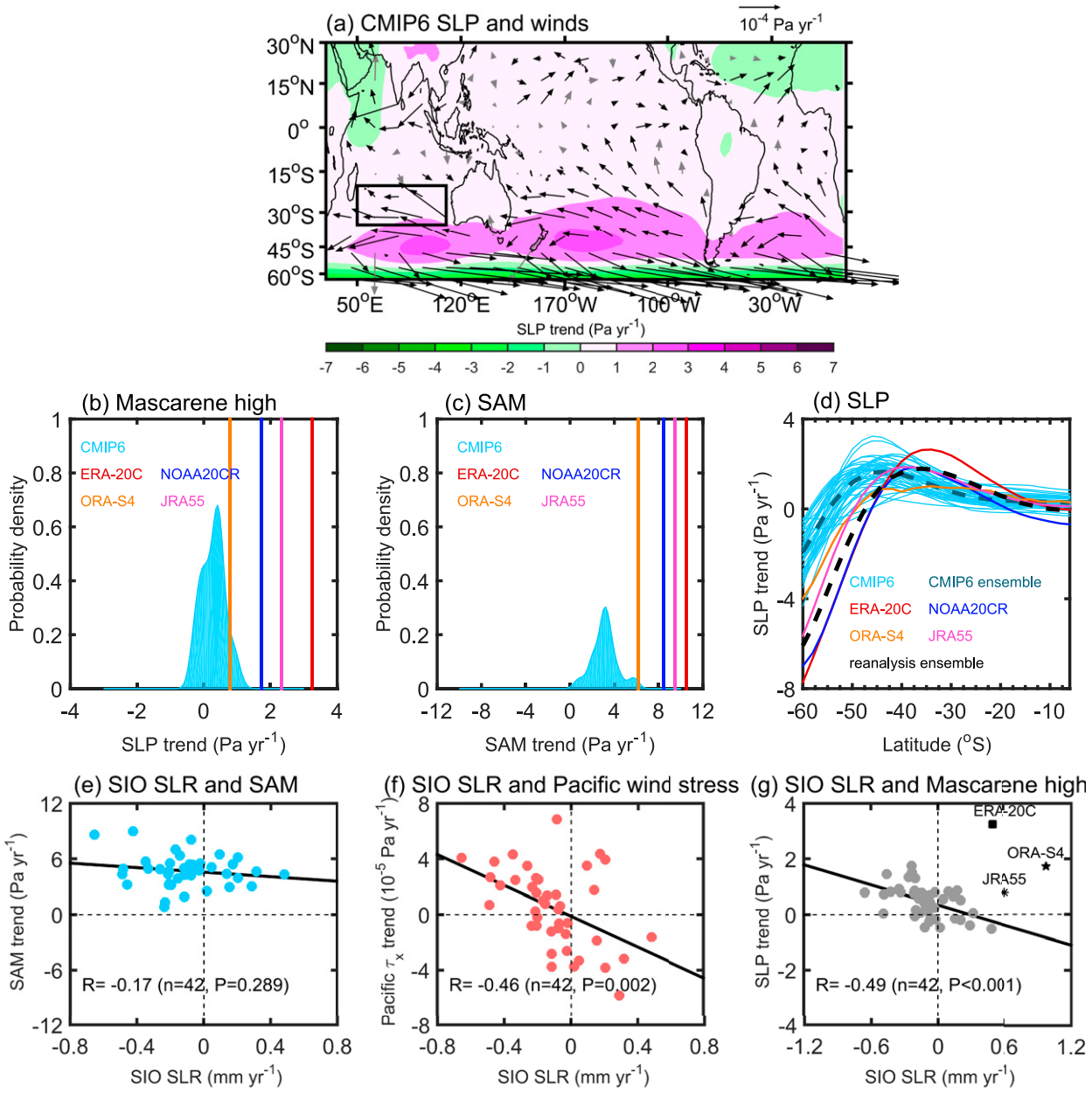

FIG. 10. Trends of SLP and surface winds in climate models. (a) Linear trends of surface wind stress (arrows; in Pa yr^{-1}) and SLP (color shading; in Pa yr^{-1}) for 1958–2014 based on the ensemble mean of CMIP6. Zonal wind stress trends below the 90% confidence level are plotted as gray arrows, and the values on land are not shown. Probability density distributions of the (b) Mascarene high trend and (c) SAM trend (Pa yr^{-1}) for 1958–2014 based on CMIP6 simulations. Straight lines mark the trends derived from atmospheric datasets. (d) Zonal-mean (0°–360°E) SLP trends for 1958–2014 derived from climate models and atmospheric datasets. Trends from ERA-20C and NOAA 20CR are for 1958–2010 and 1958–2012, respectively. Scatterplots of (e) the SIO SLR (mm yr^{-1}) vs SAM trends, (f) the SIO SLR vs the western Pacific zonal wind stress (τ_x; 20°S–20°N, 120°E–180°; as a proxy for the Pacific Walker circulation) trends, and (g) the SIO SLR vs the Mascarene high trends. Results from ERA-20C, ORA-S4, and JRA-55 are also shown in (g) and the SIO SLR rates for ERA-20C and JRA-55 are based on LICOM3–0.1° and LICOM3°–1°, respectively. The significance of the correlation is determined by a two-tailed *t*-test.

Atlantic may differ from that of the SIO and demands particular investigations. The underestimation of SLP trends is seen in the entire SH subtropical band (Fig. 11), which is the primary cause for the overlooked regional SLR in climate models (Fig. 1). Among the three basins, the trends in the South Atlantic Ocean are subjected to a larger degree of uncertainty. There is a notable spread of the SLP trends among atmospheric reanalysis datasets, and the trends from NOAA 20CR and JRA-55 are weaker than that of the CMIP6 ensemble mean (Fig. 11c). The large

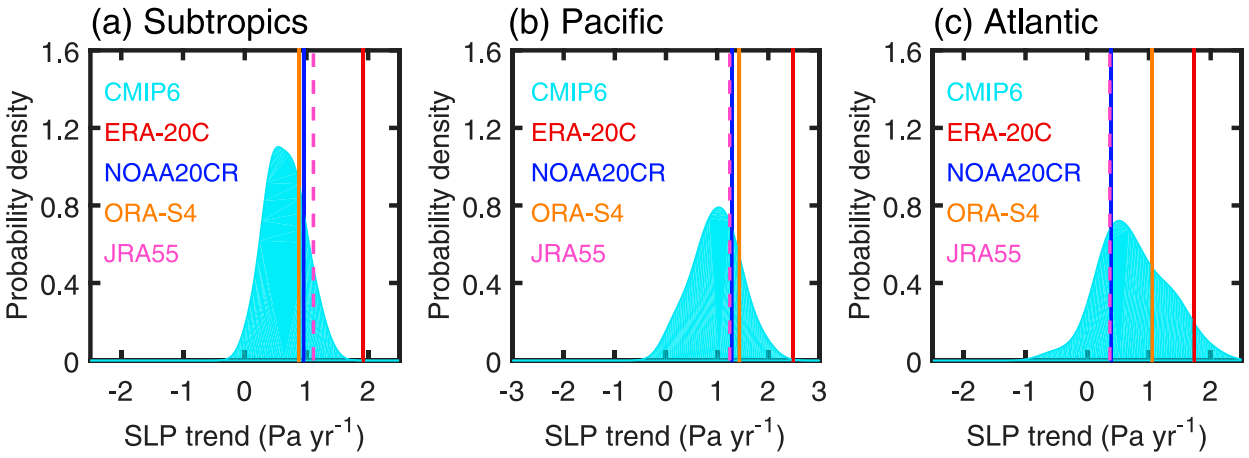

FIG. 11. SLP trends in climate models. Probability density distributions of the 1958–2014 SLP trends for (a) the subtropics of the SH (35°–20°S), (b) the southern Pacific Ocean (35°–20°S, 150°E–130°W), and (c) the southern Atlantic Ocean (35°–20°S, 40°W–0°) derived from CMIP6 simulations. Straight lines mark the trends derived from atmospheric datasets. Trends from ERA-20C and NOAA 20CR are for 1958–2010 and 1958–2012, respectively.

uncertainty in atmospheric datasets makes it more difficult to quantify model errors.

Differing from the SIO, the model–data differences in the Pacific and Atlantic Oceans may partly arise from internal variability. For example, low-frequency natural variability of the Atlantic climate, such as the Atlantic multidecadal oscillation, may also play a role in dictating the observed SLP and SLR trends in the South Atlantic since 1958. With regard to the effects of the tropical Pacific and Atlantic Oceans, we have also preliminarily examined the intensity changes of Hadley cells (figures not shown) and found that Pacific Hadley cell shows significant weakening (strengthening) trend in NOAA 20CR (ERA-20C, ORA-S4, and JRA-55) and Atlantic Hadley cell show significant (insignificant) strengthening trend in ORA-S4 and JRA-55 (ERA-20C and NOAA 20CR) at 95% confidence. Due to these uncertainties and competing processes, we are currently unable to draw conclusions for the Pacific and Atlantic Oceans.

Our numerical experimental results show that local wind changes are the dominant factor on the long-term SLR rates (>50 years) in the SIO, which is not in conflict with previous studies that attribute SLR to ITF changes (e.g., Zhuang et al. 2013; Lee et al. 2015; Li et al. 2017; Zhang et al. 2018; Jyoti et al. 2019; Nagura and McPhaden 2021). These studies mainly focused on interannual to interdecadal time scales. For example, Nagura and McPhaden (2021) found that sea level variability at midlatitudes of the south Indian Ocean is mainly driven by ENSO, in which SLAs are excited in the Pacific Ocean and propagates into the SIO through the ITF; Jyoti et al. (2019) found that the SLR in the SIO is faster than the global mean sea level during 2000–15, and the enhanced ITF is the dominator by transporting warm and freshwater anomalies into the SIO.

It should be noted that ocean mass change (barystatic effect) also affects regional SLR. Using the F20 steric and barystatic (include effects of mass change for glaciers, Greenland and Antarctic ice sheets, and terrestrial water storage) sea level data, we examine the effect of barystatic component (Fig. 12). The results show that although the barystatic effect is not negligible for regional SLR, the steric component generally dominates the regional SLR pattern, especially for the enhanced SLR in the SH subtropics. The barystatic effect on regional SLR requires further investigation, particularly on how to synthesize the observation-based barystatic sea level change with the dynamical sea level change in models to facilitate sea level prediction/projection. This study mainly worked on basin-average SLR without appreciating the SLR structure in each basin, which can, to some extent, reduce the uncertainty in SLR estimation from observation data sampling. However, our results also suggest discernible east–west contrasts in three basins (Figs. 1 and 2). For example, the SLR trends are positive and negative in the western and eastern Pacific basins, respectively. This may be related to the redistribution by the subtropical gyre circulation and the eastern boundary forcing (e.g., Qiu and Chen 2006; Roemmich et al. 2016). Our model experiments demonstrate that local wind changes related to the SAM can induce the rapid rise of the basin-mean sea level in the SH subtropics between 35° and 20°S. Yet, the east–west contrast requires further investigation, considering its linkages to ocean circulation and regional climate.

Our results suggest that the observed SH subtropical SLR is largely driven by the upward SAM trend associated with ozone depletion (e.g., Cai and Cowan 2007; Thompson et al. 2011). Given this, there might be mitigation of SLR over the coming decades, owing to the recovery of Antarctic ozone depletion (Polvani et al. 2011). Nevertheless, forced by the increasing emissions of greenhouse gases, the future SLR is expected to be continuously rapid in the SH subtropics, with increasing severity and seriousness of the threat to surrounding countries. The probabilistic prediction of regional SLR is essential for formulating adaption strategies, which rely largely upon climate models (e.g., Oppenheimer et al. 2019; Slangen et al. 2017; Hauer et al. 2020). To improve the model representation

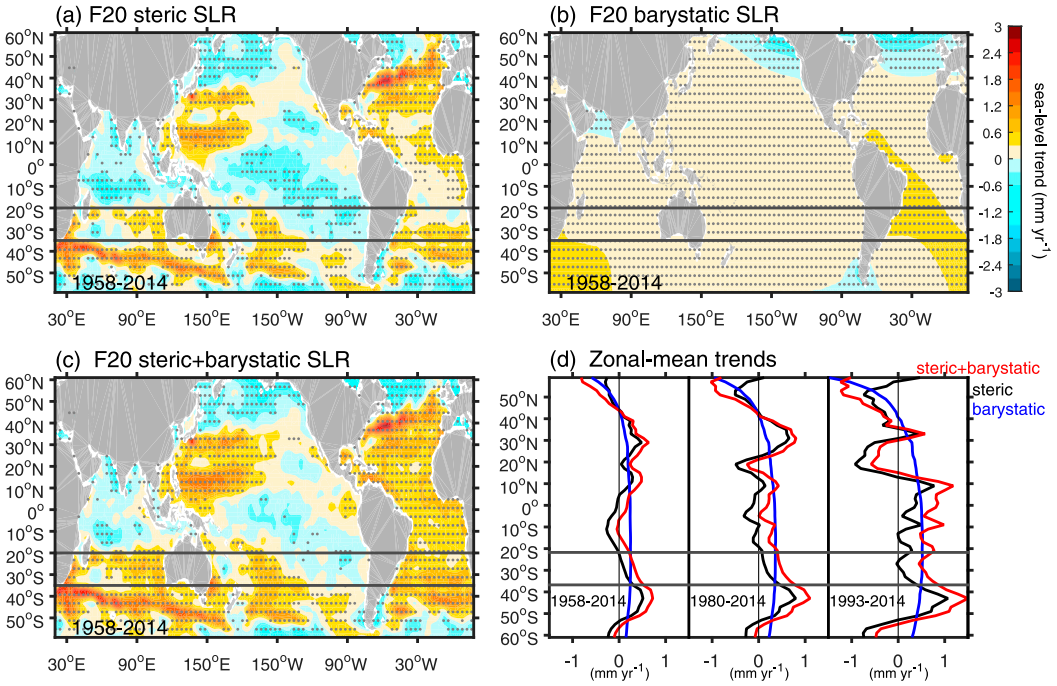

FIG. 12. Regional sea level trend patterns from F20. Linear sea level trends (mm yr^{-1}) for 1958–2014 based on (a) F20 steric sea level, (b) F20 barystatic sea level, and (c) the sum of steric and barystatic sea level. To obtain the regional sea level, the global-mean sea level time series has been removed. The black lines indicate the latitudinal range of the SH subtropics (35°–20°S). Stippling indicates significant trends at the 95% confidence level based on a Mann–Kendall test. (d) Zonal-mean (0°–360°E) sea level trends in the SH for the periods of 1958–2014, 1980–2014, and 1993–2014 derived from steric sea level, barystatic sea level, and total sea level (steric plus barystatic) of F20.

of the SLR over the SH oceans, some steps seem to be requisite, such as using more realistic ozone forcing (Neely et al. 2014), reducing biases in the Southern Ocean climatology (Wang et al. 2014), better taking into account small-scale eddies (Böning et al. 2008). Overall, these results have important implications for understanding and predicting regional SLR in the ongoing anthropogenic climate change, and this work contributes to helping the hundreds of millions of people residing in coastal areas of South America, Africa, and Australia adapt to future global climate change, with implications for other areas of the world.

Acknowledgments. We thank Wenju Cai for helpful suggestions on the earlier version of the manuscript. Three anonymous reviewers provided insightful comments for this work. This research is jointly supported by the National Key R&D Program of China under Grant 2019YFA0606702, the Strategic Priority Research Program of Chinese Academy of Sciences under Grants XDB42000000 and 40000000, the Shandong Provincial Natural Science Foundation under Grant ZR2020JQ17, and Key Deployment Project of CAS Centre for Ocean Mega-Science under Grant COMS2019Q07. Portions of this study were supported by the Regional and Global Model Analysis (RGMA) component of the Earth and Environmental System Modeling Program of the U.S. Department of Energy's Office of Biological and Environmental Research (BER) via National Science Foundation IA 1947282, and also by the National Center for Atmospheric Research (NCAR), which is a major facility sponsored by the NSF under Cooperative Agreement 1852977. W. Han and L. Zhang are supported by NSF AGS 1935279.

Data availability statement. F20 steric and barystatic sea level anomalies and global-mean total sea level time series can be obtained from https://zenodo.org/record/3862995#.X0eVdFlzaUm. IAP steric sea-level anomaly data can be found at Lijing Cheng's website: http://www.ocean.iap.ac.cn/. WOA steric sea-level anomaly data can be downloaded at https://www.nodc.noaa.gov/OC5/indprod.html. Temperature and salinity data of EN4 and Ishii are obtained from https://www.metoffice.gov.uk/hadobs/en4/download-en4-2-1.html and https://www.data.jma.go.jp/gmd/kaiyou/english/ohc/ohc_global_en.html. Sea-level, wind data, and SLP data of ORA-S4 are downloaded from http://apdrc.soest.hawaii.edu/datadoc/ecmwf_oras4.php and https://apps.ecmwf.int/datasets/. ORA-S5 and GECCO3 sea level can be downloaded at https://www.cen.uni-hamburg.de/icdc/data/ocean.html. OFES sea level can be found at http://apdrc.soest.hawaii.edu/datadoc/ofes/ofes.php. LICOM3-1° sea level can be downloaded at http://esg.lasg.ac.cn/thredds/fileServer/esg_dataroot/CMIP6/OMIP/CAS/FGOALS-f3-L/omip2/r1i1p1f1/Omon/zos/gn/v20191104/zos_Omon_FGOALS-f3-L_omip2_r1i1p1f1_gn_165301-201812.nc. LICOM3-0.1° sea level data are available upon request (Pengfei Lin; linpf@mail.iap.ac.cn). ERA-20C wind and SLP data are

downloaded from https://apps.ecmwf.int/datasets/. Wind and SLP data of NOAA 20CR are obtained from NOAA's PSD website at https://www.esrl.noaa.gov/psd/data/gridded/. JRA-55 wind and SLP data are downloaded at https://rda.ucar.edu/datasets/ds628.1/#!description. CMIP6 datasets are available at https://esgf-node.llnl.gov/projects/cmip6/. CMIP5 datasets can be downloaded at http://cmip-pcmdi.llnl.gov/cmip5/. CESM-LE simulations can be obtained from https://www.earthsystemgrid.org/dataset/ucar.cgd.ccsm4.output.html. AVISO data are available at https://www.aviso.altimetry.fr/en/home.html. Codes for HYCOM can be downloaded from https:/www.hycom.org/. All codes for analysis and figure creation are available upon request.

REFERENCES

Alexander, M. A., I. Bladé, M. Newman, J. R. Lanzante, N. C. Lau, and J. D. Scott, 2002: The atmospheric bridge: The influence of ENSO teleconnections on air–sea interaction over the global oceans. *J. Climate*, **15**, 2205–2231, https://doi.org/10.1175/1520-0442(2002)015<2205:TABTIO>2.0.CO;2.

Balmaseda, M. A., K. Mogensen, and A. T. Weaver, 2013: Evaluation of the ECMWF ocean reanalysis system ORAS4. *Quart. J. Roy. Meteor. Soc.*, **139**, 1132–1161, https://doi.org/10.1002/qj.2063.

Bleck, R., 2002: An oceanic general circulation model framed in hybrid isopycnic-Cartesian coordinates. *Ocean Modell.*, **4**, 55–88, https://doi.org/10.1016/S1463-5003(01)00012-9.

Böning, C. W., A. Dispert, M. Visbeck, S. R. Rintoul, and F. U. Schwarzkopf, 2008: The response of the Antarctic Circumpolar Current to recent climate change. *Nat. Geosci.*, **1**, 864–869, https://doi.org/10.1038/ngeo362.

Bouttes, N., J. M. Gregory, T. Kuhlbrodt, and T. Suzuki, 2012: The effect of windstress change on future sea level change in the Southern Ocean. *Geophys. Res. Lett.*, **39**, L23602, https://doi.org/10.1029/2012GL054207.

Cai, W., and T. Cowan, 2007: Trends in Southern Hemisphere circulation in IPCC AR4 models over 1950–99: Ozone depletion versus greenhouse forcing. *J. Climate*, **20**, 681–693, https://doi.org/10.1175/JCLI4028.1.

——, ——, S. Godfrey, and S. Wijffels, 2010: Simulations of processes associated with the fast warming rate of the southern midlatitude ocean. *J. Climate*, **23**, 197–206, https://doi.org/10.1175/2009JCLI3081.1.

——, and Coauthors, 2019: Pantropical climate interactions. *Science*, **363**, eaav4236, https://doi.org/10.1126/science.aav4236.

Chambers, D. P., M. A. Merrifield, and R. S. Nerem, 2012: Is there a 60-year oscillation in global mean sea level? *Geophys. Res. Lett.*, **39**, L18607, https://doi.org/10.1029/2012GL052885.

Cheng, L., and Coauthors, 2016: XBT science: Assessment of instrumental biases and errors. *Bull. Amer. Meteor. Soc.*, **97**, 923–933, https://doi.org/10.1175/BAMS-D-15-00031.1.

——, K. E. Trenberth, J. Fasullo, T. Boyer, J. Abraham, and J. Zhu, 2017: Improved estimates of ocean heat content from 1960 to 2015. *Sci. Adv.*, **3**, e1601545, https://doi.org/10.1126/sciadv.1601545.

Compo, G. P., and Coauthors, 2011: The Twentieth Century Reanalysis Project. *Quart. J. Roy. Meteor. Soc.*, **137** (654), 1–28, https://doi.org/10.1002/qj.776.

Dangendorf, S., C. Hay, F. M. Calafat, M. Marcos, C. G. Piecuch, K. Berk, and J. Jensen, 2019: Persistent acceleration in global sea-level rise since the 1960s. *Nat. Climate Change*, **9**, 705–710, https://doi.org/10.1038/s41558-019-0531-8.

Dee, D. P., and Coauthors, 2011: The ERA-Interim reanalysis: Configuration and performance of the data assimilation system. *Quart. J. Roy. Meteor. Soc.*, **137**, 553–597, https://doi.org/10.1002/qj.828.

Du, Y., and S.-P. Xie, 2008: Role of atmospheric adjustments in the tropical Indian Ocean warming during the 20th century in climate models. *Geophys. Res. Lett.*, **35**, L08712, https://doi.org/10.1029/2008GL033631.

Duan, J., Y. Li, L. Zhang, and F. Wang, 2020: Impacts of the Indian Ocean dipole on sea level and gyre circulation of the western tropical Pacific Ocean. *J. Climate*, **33**, 4207–4228, https://doi.org/10.1175/JCLI-D-19-0782.1.

Duvat, V. K. E., 2019: A global assessment of atoll island planform changes over the past decades. *Wiley Interdiscip. Rev. Climate Change*, **10**, e557, https://doi.org/10.1002/wcc.557.

Eyring, V., and Coauthors, 2013: Long-term ozone changes and associated climate impacts in CMIP5 simulations. *J. Geophys. Res. Atmos.*, **118**, 5029–5060, https://doi.org/10.1002/jgrd.50316.

——, S. Bony, G. A. Meehl, C. A. Senior, B. Stevens, R. J. Stouffer, and K. E. Taylor, 2016: Overview of the Coupled Model Intercomparison Project Phase 6 (CMIP6) experimental design and organization. *Geosci. Model Dev.*, **9**, 1937–1958, https://doi.org/10.5194/gmd-9-1937-2016.

Fairall, C. W., E. F. Bradley, J. E. Hare, A. A. Grachev, and J. B. Edson, 2003: Bulk parameterization of air–sea fluxes: Updates and verification for the COARE algorithm. *J. Climate*, **16**, 571–591, https://doi.org/10.1175/1520-0442(2003)016<0571:BPOASF>2.0.CO;2.

Feng, M., 2004: Multidecadal variations of Fremantle sea level: Footprint of climate variability in the tropical Pacific. *Geophys. Res. Lett.*, **31**, L16302, https://doi.org/10.1029/2004GL019947.

Frankcombe, L. M., P. Spence, A. M. Hogg, M. H. England, and S. M. Griffies, 2013: Sea level changes forced by Southern Ocean winds. *Geophys. Res. Lett.*, **40**, 5710–5715, https://doi.org/10.1002/2013GL058104.

Frederikse, T., and Coauthors, 2020: The causes of sea-level rise since 1900. *Nature*, **584**, 393–397, https://doi.org/10.1038/s41586-020-2591-3.

——, and Coauthors, 2021: Constraining 20th-century sea-level rise in the South Atlantic Ocean. *J. Geophys. Res. Oceans*, **126**, e2020JC016970, https://doi.org/10.1029/2020JC016970.

Giese, B. S., and S. Ray, 2011: El Niño variability in simple ocean data assimilation (SODA), 1871–2008. *J. Geophys. Res.*, **116**, C02024, https://doi.org/10.1029/2010JC006695.

Gong, D., and S. Wang, 1998: Antarctic oscillation: Concept and applications. *Chinese Sci. Bull.*, **43**, 734–738, https://doi.org/10.1007/BF02898949.

Good, S. A., M. J. Martin, and N. A. Rayner, 2013: EN4: Quality controlled ocean temperature and salinity profiles and monthly objective analyses with uncertainty estimates. *J. Geophys. Res. Oceans*, **118**, 6704–6716, https://doi.org/10.1002/2013JC009067.

Griffies, S. M., and Coauthors, 2016: OMIP contribution to CMIP6: Experimental and diagnostic protocol for the physical component of the Ocean Model Intercomparison Project. *Geosci. Model Dev.*, **9**, 3231–3296, https://doi.org/10.5194/gmd-9-3231-2016.

Han, W., and Coauthors, 2010: Patterns of Indian Ocean sea-level change in a warming climate. *Nat. Geosci.*, **3**, 546–550, https://doi.org/10.1038/ngeo901.

——, and Coauthors, 2014: Intensification of decadal and multi-decadal sea level variability in the western tropical Pacific during recent decades. *Climate Dyn.*, **43**, 1357–1379, https://doi.org/10.1007/s00382-013-1951-1.

Hauer, M. E., E. Fussell, V. Mueller, M. Burkett, M. Call, K. Abel, R. McLeman, and D. Wrathall, 2020: Sea-level rise and human migration. *Nat. Rev. Earth Environ.*, **1**, 28–39, https://doi.org/10.1038/s43017-019-0002-9.

Hay, C. C., E. Morrow, R. E. Kopp, and J. X. Mitrovica, 2015: Probabilistic reanalysis of twentieth-century sea-level rise. *Nature*, **517**, 481–484, https://doi.org/10.1038/nature14093.

Hurrell, J. W., and Coauthors, 2013: The Community Earth System Model: A framework for collaborative research. *Bull. Amer. Meteor. Soc.*, **94**, 1339–1360, https://doi.org/10.1175/BAMS-D-12-00121.1.

Hwang, Y.-T., and D. M. W. Frierson, 2013: Link between the double-Intertropical Convergence Zone problem and cloud biases over the southern Ocean. *Proc. Natl. Acad. Sci. USA*, **110**, 4935–4940, https://doi.org/10.1073/pnas.1213302110.

Ishii, M., Y. Fukuda, S. Hirahara, S. Yasui, T. Suzuki, and K. Sato, 2017: Accuracy of global upper ocean heat content estimation expected from present observational data sets. *SOLA*, **13**, 163–167, https://doi.org/10.2151/sola.2017-030.

Jevrejeva, S., A. Grinsted, and J. C. Moore, 2014: Upper limit for sea level projections by 2100. *Environ. Res. Lett.*, **9**, 104008, https://doi.org/10.1088/1748-9326/9/10/104008.

Jyoti, J., P. Swapna, R. Krishnan, and C. V. Naidu, 2019: Pacific modulation of accelerated south Indian Ocean sea level rise during the early 21st century. *Climate Dyn.*, **53**, 4413–4432, https://doi.org/10.1007/s00382-019-04795-0.

Kara, A. B., H. E. Hurlburt, and A. J. Wallcraft, 2005: Stability-dependent exchange coefficients for air–sea fluxes. *J. Atmos. Oceanic Technol.*, **22**, 1080–1094, https://doi.org/10.1175/JTECH1747.1.

Kay, J. E., and Coauthors, 2015: The Community Earth System Model (CESM) large ensemble project: A community resource for studying climate change in the presence of internal climate variability. *Bull. Amer. Meteor. Soc.*, **96**, 1333–1349, https://doi.org/10.1175/BAMS-D-13-00255.1.

Knutson, T. R., and J. Ploshay, 2021: Sea level pressure trends: Model-based assessment of detection, attribution, and consistency with CMIP5 historical simulations. *J. Climate*, **34**, 327–346, https://doi.org/10.1175/JCLI-D-19-0997.1.

Kobayashi, S., and Coauthors, 2015: The JRA-55 reanalysis: General specifications and basic characteristics. *J. Meteor. Soc. Japan*, **93**, 5–48, https://doi.org/10.2151/jmsj.2015-001.

Köhl, A., 2020: Evaluating the GECCO3 1948–2018 ocean synthesis—A configuration for initializing the MPI-ESM climate model. *Quart. J. Roy. Meteor. Soc.*, **146**, 2250–2273, https://doi.org/10.1002/qj.3790.

Kumar, P., B. Hamlington, S. Cheon, W. Han, and P. Thompson, 2020: 20th century multivariate Indian Ocean regional sea level reconstruction. *J. Geophys. Res. Oceans*, **125**, e2020JC016270, https://doi.org/10.1029/2020JC016270.

Lau, W. K. M., and K.-M. Kim, 2015: Robust Hadley circulation changes and increasing global dryness due to CO_2 warming from CMIP5 model projections. *Proc. Natl. Acad. Sci. USA*, **112**, 3630–3635, https://doi.org/10.1073/pnas.1418682112.

Lee, S.-K., W. Park, M. O. Baringer, A. L. Gordon, B. Huber, and Y. Liu, 2015: Pacific origin of the abrupt increase in Indian Ocean heat content during the warming hiatus. *Nat. Geosci.*, **8**, 445–449, https://doi.org/10.1038/ngeo2438.

Lee, T., and M. J. McPhaden, 2008: Decadal phase change in large-scale sea level and winds in the Indo-Pacific region at the end of the 20th century. *Geophys. Res. Lett.*, **35**, L01605, https://doi.org/10.1029/2007GL032419.

Le Traon, P. Y., F. Nadal, and N. Ducet, 1998: An improved mapping method of multisatellite altimeter data. *J. Atmos. Oceanic Technol.*, **15**, 522–534, https://doi.org/10.1175/1520-0426(1998)015<0522:AIMMOM>2.0.CO;2.

Levitus, S., and Coauthors, 2012: World Ocean heat content and thermosteric sea level change (0–2000 m), 1955–2010. *Geophys. Res. Lett.*, **39**, L10603, https://doi.org/10.1029/2012GL051106.

Li, M., A. L. Gordon, J. Wei, L. K. Gruenburg, and G. Jiang, 2018: Multi-decadal timeseries of the Indonesian Throughflow. *Dyn. Atmos. Oceans*, **81**, 84–95, https://doi.org/10.1016/j.dynatmoce.2018.02.001.

Li, Y., and W. Han, 2015: Decadal sea level variations in the Indian Ocean investigated with HYCOM: Roles of climate modes, ocean internal variability, and stochastic wind forcing. *J. Climate*, **28**, 9143–9165, https://doi.org/10.1175/JCLI-D-15-0252.1.

——, ——, and L. Zhang, 2017: Enhanced decadal warming of the southeast Indian Ocean during the recent global surface warming slowdown. *Geophys. Res. Lett.*, **44**, 9876–9884, https://doi.org/10.1002/2017GL075050.

——, ——, A. Hu, G. A. Meehl, and F. Wang, 2018: Multidecadal changes of the upper Indian Ocean heat content during 1965–2016. *J. Climate*, **31**, 7863–7884, https://doi.org/10.1175/JCLI-D-18-0116.1.

——, and Coauthors, 2020: Eddy-resolving simulation of CAS-LICOM3 for phase 2 of the Ocean Model Intercomparison Project. *Adv. Atmos. Sci.*, **37**, 1067–1080, https://doi.org/10.1007/s00376-020-0057-z.

Lin, P., and Coauthors, 2020: LICOM model datasets for the CMIP6 Ocean Model Intercomparison Project. *Adv. Atmos. Sci.*, **37**, 239–249, https://doi.org/10.1007/s00376-019-9208-5.

Liu, Q. Y., M. Feng, D. Wang, and S. Wijffels, 2015: Interannual variability of the Indonesian Throughflow transport: A revisit based on 30 year expendable bathythermograph data. *J. Geophys. Res. Oceans*, **120**, 8270–8282, https://doi.org/10.1002/2015JC011351.

Llovel, W., and T. Lee, 2015: Importance and origin of halosteric contribution to sea level change in the southeast Indian Ocean during 2005–2013. *Geophys. Res. Lett.*, **42**, 1148–1157, https://doi.org/10.1002/2014GL062611.

——, and L. Terray, 2016: Observed southern upper-ocean warming over 2005–2014 and associated mechanisms. *Environ. Res. Lett.*, **11**, 124023, https://doi.org/10.1088/1748-9326/11/12/124023.

——, I. Fukumori, and B. Meyssignac, 2013: Depth-dependent temperature change contributions to global mean thermosteric sea level rise from 1960 to 2010. *Global Planet. Change*, **101**, 113–118, https://doi.org/10.1016/j.gloplacha.2012.12.011.

Lyu, K., X. Zhang, J. A. Church, and Q. Wu, 2020: Processes responsible for the Southern Hemisphere ocean heat uptake and redistribution under anthropogenic warming. *J. Climate*, **33**, 3787–3807, https://doi.org/10.1175/JCLI-D-19-0478.1.

Merrifield, M. A., 2011: A shift in western tropical Pacific sea level trends during the 1990s. *J. Climate*, **24**, 4126–4138, https://doi.org/10.1175/2011JCLI3932.1.

Meyers, G., 1996: Variation of Indonesian Throughflow and the El Niño–Southern Oscillation. *J. Geophys. Res.*, **101**, 12 255–12 263, https://doi.org/10.1029/95JC03729.

Meyssignac, B., M. Becker, W. Llovel, and A. Cazenave, 2012: An assessment of two-dimensional past sea level reconstructions over 1950–2009 based on tide-gauge data and different input sea level grids. *Surv. Geophys.*, **33**, 945–972, https://doi.org/10.1007/s10712-011-9171-x.

Milne, G. A., W. R. Gehrels, C. W. Hughes, and M. E. Tamisiea, 2009: Identifying the causes of sea-level change. *Nat. Geosci.*, **2**, 471–478, https://doi.org/10.1038/ngeo544.

Mitas, C. M., 2005: Has the Hadley cell been strengthening in recent decades? *Geophys. Res. Lett.*, **32**, L03809, https://doi.org/10.1029/2004GL021765.

Nagura, M., and M. J. McPhaden, 2021: Interannual variability in sea surface height at southern midlatitudes of the Indian Ocean. *J. Phys. Oceanogr.*, **51**, 1595–1609, https://doi.org/10.1175/JPO-D-20-0279.1.

Neely, R. R., D. R. Marsh, K. L. Smith, S. M. Davis, and L. M. Polvani, 2014: Biases in Southern Hemisphere climate trends induced by coarsely specifying the temporal resolution of stratospheric ozone. *Geophys. Res. Lett.*, **41**, 8602–8610, https://doi.org/10.1002/2014GL061627.

Nguyen, H., A. Evans, C. Lucas, I. Smith, and B. Timbal, 2013: The Hadley circulation in reanalyses: Climatology, variability, and change. *J. Climate*, **26**, 3357–3376, https://doi.org/10.1175/JCLI-D-12-00224.1.

Oppenheimer, M., and Coauthors, 2019: Sea level rise and implications for low lying islands, coasts and communities. *IPCC Special Report on the Ocean and Cryosphere in a Changing Climate*, H.-O. Pörtner et al., Eds., Cambridge University Press, 321–445.

Pierce, D. W., P. J. Gleckler, T. P. Barnett, B. D. Santer, and P. J. Durack, 2012: The fingerprint of human-induced changes in the ocean's salinity and temperature fields. *Geophys. Res. Lett.*, **39**, L21704, https://doi.org/10.1029/2012GL053389..

Poli, P., and Coauthors, 2016: ERA-20C: An atmospheric reanalysis of the twentieth century. *J. Climate*, **29**, 4083–4097, https://doi.org/10.1175/JCLI-D-15-0556.1.

Polvani, L. M., M. Previdi, and C. Deser, 2011: Large cancellation, due to ozone recovery, of future Southern Hemisphere atmospheric circulation trends. *Geophys. Res. Lett.*, **38**, L04707, https://doi.org/10.1029/2011GL046712.

Qiu, B., and S. Chen, 2006: Decadal variability in the large-scale sea surface height field of the South Pacific Ocean: Observations and causes. *J. Phys. Oceanogr.*, **36**, 1751–1762, https://doi.org/10.1175/JPO2943.1.

——, and ——, 2012: Multidecadal sea level and gyre circulation variability in the northwestern tropical Pacific Ocean. *J. Phys. Oceanogr.*, **42**, 193–206, https://doi.org/10.1175/JPO-D-11-061.1.

——, ——, L. Wu, and S. Kida, 2015: Wind- versus eddy-forced regional sea level trends and variability in the North Pacific Ocean. *J. Climate*, **28**, 1561–1577, https://doi.org/10.1175/JCLI-D-14-00479.1.

Qu, T., I. Fukumori, and R. A. Fine, 2019: Spin-up of the Southern Hemisphere super gyre. *J. Geophys. Res. Oceans*, **124**, 154–170, https://doi.org/10.1029/2018JC014391.

Roemmich, D., J. Church, J. Gilson, D. Monselesan, P. Sutton, and S. Wijffels, 2015: Unabated planetary warming and its ocean structure since 2006. *Nat. Climate Change*, **5**, 240–245, https://doi.org/10.1038/nclimate2513.

——, J. Gilson, P. Sutton, and N. Zilberman, 2016: Multidecadal change of the South Pacific gyre circulation. *J. Phys. Oceanogr.*, **46**, 1871–1883, https://doi.org/10.1175/JPO-D-15-0237.1.

Roxy, M. K., K. Ritika, P. Terray, and S. Masson, 2014: The curious case of Indian Ocean warming. *J. Climate*, **27**, 8501–8509, https://doi.org/10.1175/JCLI-D-14-00471.1.

Sasaki, H., M. Nonaka, Y. Masumoto, Y. Sasai, H. Uehara, and H. Sakuma, 2008: An eddy-resolving hindcast simulation of the quasiglobal ocean from 1950 to 2003 on the Earth Simulator. *High Resolution Numerical Modelling of the Atmosphere and Ocean*, K. Hamilton and W. Ohfuchi, Eds., Springer, 157–185.

Schwarzkopf, F. U., and C. W. Böning, 2011: Contribution of Pacific wind stress to multi-decadal variations in upper-ocean heat content and sea level in the tropical south Indian Ocean. *Geophys. Res. Lett.*, **38**, L12602, https://doi.org/10.1029/2011GL047651.

Sérazin, G., B. Meyssignac, T. Penduff, L. Terray, B. Barnier, and J.-M. Molines, 2016: Quantifying uncertainties on regional sea level change induced by multidecadal intrinsic oceanic variability. *Geophys. Res. Lett.*, **43**, 8151–8159, https://doi.org/10.1002/2016GL069273.

Slangen, A. B. A., F. Adloff, S. Jevrejeva, P. W. Leclercq, B. Marzeion, Y. Wada, and R. Winkelmann, 2017: A review of recent updates of sea-level projections at global and regional scales. *Surv. Geophys.*, **38**, 385–406, https://doi.org/10.1007/s10712-016-9374-2.

Sprintall, J., and A. Révelard, 2014: The Indonesian Throughflow response to Indo-Pacific climate variability. *J. Geophys. Res. Oceans*, **119**, 1161–1175, https://doi.org/10.1002/2013JC009533.

——, S. E. Wijffels, R. Molcard, and I. Jaya, 2009: Direct estimates of the Indonesian Throughflow entering the Indian Ocean: 2004–2006. *J. Geophys. Res.*, **114**, C07001, https://doi.org/10.1029/2008JC005257.

——, A. L. Gordon, A. Koch-Larrouy, T. Lee, J. T. Potemra, K. Pujiana, and S. E. Wijffels, 2014: The Indonesian seas and their role in the coupled ocean–climate system. *Nat. Geosci.*, **7**, 487–492, https://doi.org/10.1038/ngeo2188.

Stammer, D., and S. Hüttemann, 2008: Response of regional sea level to atmospheric pressure loading in a climate change scenario. *J. Climate*, **21**, 2093–2101, https://doi.org/10.1175/2007JCLI1803.1.

Stevenson, D. S., and Coauthors, 2013: Tropospheric ozone changes, radiative forcing and attribution to emissions in the Atmospheric Chemistry and Climate Model Intercomparison Project (ACCMIP). *Atmos. Chem. Phys.*, **13**, 3063–3085, https://doi.org/10.5194/acp-13-3063-2013.

Susanto, R. D., and Y. T. Song, 2015: Indonesian Throughflow proxy from satellite altimeters and gravimeters. *J. Geophys. Res. Oceans*, **120**, 2844–2855, https://doi.org/10.1002/2014JC010382.

Swart, N. C., and J. C. Fyfe, 2012: Observed and simulated changes in the Southern Hemisphere surface westerly wind-stress. *Geophys. Res. Lett.*, **39**, L16711, https://doi.org/10.1029/2012GL052810.

Taylor, K. E., R. J. Stouffer, and G. A. Meehl, 2012: An overview of CMIP5 and the experiment design. *Bull. Amer. Meteor. Soc.*, **93**, 485–498, https://doi.org/10.1175/BAMS-D-11-00094.1.

Thompson, D. W. J., S. Solomon, P. J. Kushner, M. H. England, K. M. Grise, and D. J. Karoly, 2011: Signatures of the Antarctic ozone hole in Southern Hemisphere surface climate change. *Nat. Geosci.*, **4**, 741–749, https://doi.org/10.1038/ngeo1296.

Thompson, P. R., and M. A. Merrifield, 2014: A unique asymmetry in the pattern of recent sea level change. *Geophys. Res. Lett.*, **41**, 7675–7683, https://doi.org/10.1002/2014GL061263.

Tokinaga, H., S.-P. Xie, C. Deser, Y. Kosaka, and Y. M. Okumura, 2012: Slowdown of the Walker circulation driven by tropical Indo-Pacific warming. *Nature*, **491**, 439–443, https://doi.org/10.1038/nature11576.

Trenary, L. L., and W. Han, 2013: Local and remote forcing of decadal sea level and thermocline depth variability in the south Indian Ocean. *J. Geophys. Res. Oceans*, **118**, 381–398, https://doi.org/10.1029/2012JC008317.

Trenberth, K. E., 1979: Interannual variability of the 500 mb zonal mean flow in the Southern Hemisphere. *Mon. Wea. Rev.*, **107**, 1515–1524, https://doi.org/10.1175/1520-0493(1979)107<1515:IVOTMZ>2.0.CO;2.

Tsujino, H., and Coauthors, 2018: JRA-55 based surface dataset for driving ocean–sea-ice models (JRA55-do). *Ocean Modell.*, **130**, 79–139, https://doi.org/10.1016/j.ocemod.2018.07.002.

Uppala, S. M., and Coauthors, 2005: The ERA-40 Re-Analysis. *Quart. J. Roy. Meteor. Soc.*, **131**, 2961–3012, https://doi.org/10.1256/qj.04.176.

Vecchi, G. A., B. J. Soden, A. T. Wittenberg, I. M. Held, A. Leetmaa, and M. J. Harrison, 2006: Weakening of tropical Pacific atmospheric circulation due to anthropogenic forcing. *Nature*, **441**, 73–76, https://doi.org/10.1038/nature04744.

Vianna, M. L., and V. V. Menezes, 2013: Bidecadal sea level modes in the North and South Atlantic Oceans. *Geophys. Res. Lett.*, **40**, 5926–5931, https://doi.org/10.1002/2013GL058162.

Volkov, D. L., S.-K. Lee, F. W. Landerer, and R. Lumpkin, 2017: Decade-long deep-ocean warming detected in the subtropical South Pacific. *Geophys. Res. Lett.*, **44**, 927–936, https://doi.org/10.1002/2016GL071661.

——, ——, A. L. Gordon, and M. Rudko, 2020: Unprecedented reduction and quick recovery of the south Indian Ocean heat content and sea level in 2014–2018. *Sci. Adv.*, **6**, eabc1151, https://doi.org/10.1126/sciadv.abc1151.

Wang, C., 2019: Three-ocean interactions and climate variability: A review and perspective. *Climate Dyn.*, **53**, 5119–5136, https://doi.org/10.1007/s00382-019-04930-x.

——, L. Zhang, S.-K. Lee, L. Wu, and C. R. Mechoso, 2014: A global perspective on CMIP5 climate model biases. *Nat. Climate Change*, **4**, 201–205, https://doi.org/10.1038/nclimate2118.

Waugh, D. W., L. Oman, P. A. Newman, R. S. Stolarski, S. Pawson, J. E. Nielsen, and J. Perlwitz, 2009: Effect of zonal asymmetries in stratospheric ozone on simulated Southern Hemisphere climate trends. *Geophys. Res. Lett.*, **36**, L18701, https://doi.org/10.1029/2009GL040419.

Xue, F., H. Wang, and J. He, 2003: Interannual variability of Mascarene high and Australian high and their influences on summer rainfall over East Asia. *Chinese Sci. Bull.*, **48**, 492–497, https://doi.org/10.1007/BF03183258.

Yang, L., R. Murtugudde, L. Zhou, and P. Liang, 2020: A potential link between the Southern Ocean warming and the south Indian Ocean heat balance. *J. Geophys. Res. Oceans*, **125**, e2020JC016132, https://doi.org/10.1029/2020JC016132.

Yin, J., 2012: Century to multi-century sea level rise projections from CMIP5 models. *Geophys. Res. Lett.*, **39**, L17709, https://doi.org/10.1029/2012GL052947.

Zhang, Y., M. Feng, Y. Du, H. E. Phillips, N. L. Bindoff, and M. J. McPhaden, 2018: Strengthened Indonesian Throughflow drives decadal warming in the southern Indian Ocean. *Geophys. Res. Lett.*, **45**, 6167–6175, https://doi.org/10.1029/2018GL078265.

Zhuang, W., M. Feng, Y. Du, A. Schiller, and D. Wang, 2013: Low-frequency sea level variability in the southern Indian Ocean and its impacts on the oceanic meridional transports. *J. Geophys. Res. Oceans*, **118**, 1302–1315, https://doi.org/10.1002/jgrc.20129.

Zuo, H., M. A. Balmaseda, S. Tietsche, K. Mogensen, and M. Mayer, 2019: The ECMWF operational ensemble reanalysis–analysis system for ocean and sea ice: A description of the system and assessment. *Ocean Sci.*, **15**, 779–808, https://doi.org/10.5194/os-15-779-2019.